EXPERIMENTAL INVESTIGATION OF ON-DECK ICING FOR MARINE VESSELS

by

© Debashish Saha

A thesis submitted to the

School of Graduate Studies

in partial fulfillment of the requirements for the degree of

Masters of Engineering

Faculty of Engineering and Applied Science

Memorial University of Newfoundland

May 2017

St. John's   Newfoundland & Labrador   Canada

To my Son "Siddhartha"

ABSTRACT

Marine icing is a complex phenomenon and understanding its growth process is important to construct ice growth models that can be built with remote sensing unit as a mean of generating a more accurate ice chart that can help in the prediction and prevention of the ice accretion on the deck of the vessel/ rig. In an arctic environment, wave impact and splash can significantly affect ice accretion on a marine structure. To predict ice accretion, water sheet breakup behavior onto a surface needs to be studied closely. The freezing behavior of salt water mostly encountered in marine vessels and offshore structures is very complicated compared to fresh water due to the salt content. A comparative effort to analyze the difference and similarity between the differing ice accretion behaviors of salt and fresh water as well as to further examine water sheet splash are the motivation of experimental investigation performed in two separate lab scale test models. The setup preparation, measurement technique, and results are presented. The results show that in fresh water freezing, droplet cooling behavior, splash area and solidification time were mainly affected by the volume of the falling droplets. The presence of salt affects the cooling time as the falling droplet size is increased. The results from the water sheet breakup tests show that jet velocity significantly affects splash size upon breakup. It is also shown that high attack angles are beneficial in low-velocity impacts.

ACKNOWLEDGEMENTS

Table of Contents

List of Tables

List of Figures

Chapter 1: Introduction

1.1 Background

Marine icing can be a problem for offshore platforms and vessels working in arctic and sub-arctic conditions. Opportunities exist to enhance models for marine icing, particularly compared to atmospheric icing (Gent et al. 2000), which commonly can be anticipated by homogeneous solidifying conditions (To and Wood, 2015). From an investigation on ship icing, it was determined that the largest icing rates occur mostly during collision generated sea spray (Zakrzewski, 1987). A superior comprehension of the likely locations of major for ice accretion, that represent a hazard to human safety and vessel stability, can be determined from the mass transfer of water to a seaward marine structure/vessel (Dehghani et al., 2016; Bodaghkhani et al., 2016; Zakrzewski, 1987).

Freshwater solidification is a common and highly investigated phenomenon due to its application in the aircraft industry and power transmission lines. The freezing behavior of salt water mostly encountered in marine vessels and offshore structures, is very complicated compared to fresh water due to the salt content. Limited field simulations and experimental investigations have been conducted to understand the physics behind sea spray freezing in terms of several significant parameters (Kulyakhtin et al., 2013; Ozeki et al., 2005; Fukusako et al., 1989). With two separate experimental setups, this thesis analyzes the breakup of a flat sheet of water on a lab scale model and post-breakup sea water icing on a supercooled surface.

In this thesis, new experimental setups are designed and developed to collect data and establish new insights on the fundamentals of sea water icing, with a focus on conditions in offshore arctic and the sub-arctic locations. The experiments are conducted in the Fluids and Hydraulics Laboratory to investigate the extent of water splash and post-breakup freezing of saline droplets as they strike a supercooled surface.

1.2 Thesis objectives

The main objective of this research is to focus on two consecutive phases of collision generated sea spray icing, including (i) water sheet breakup and (ii) post-breakup droplet freezing upon impacting a solid surface.

The following requirements are fulfilled to achieve the research objectives.

- Development of an experimental apparatus to measure breakup of a water sheet on a ship bow.

- Generation of a water jet to represents high energy water delivered from a wave.

- Obtain a better estimation on water delivery to a marine structure.

- Development of an experimental facility to measure the thermal distribution and physical spreading of fresh and saline water droplets as they strike and solidify on a super-cooled surface.

- Correlation development for ice accretion behaviors of salt and fresh water.

- Analyze the presence of salt's effect on cooling time, splash area and cooling pattern for droplets.

1.3 Organization of Thesis

This thesis is organized into five chapters that follow the sequences of work performed to investigate the objectives of the study. Chapter 1 is an introduction that explains the motivation behind the study. The objectives of this experimental investigation and the contributions of the work are also presented in this chapter.

Chapter 2 presents a literature review of icing and available prevention technique in several industries. An interesting phenomenon that leads to a marine icing event, including spreading and break up of liquid sheets upon impact, solidification of atomized droplets after striking a super-cooled surface and the effect of salinity on icing are also reviewed in this chapter. Measuring and visualization techniques, as well as promising numerical modeling techniques, are also reviewed in Chapter 2.

Chapter 3 presents the two experimental setups. High-speed image acquisition and infrared image acquisition are also explained in this chapter. Chapter 4 presents and discusses the experimental results that were obtained from two different setups with specific objectives, as discussed in Section 1.2. Chapter 5 presents the conclusions and recommendations for further studies in marine icing phenomenon. Two conference papers have been published from the content of this thesis in Arctic Technology conference held in St. John's in 2016.

Chapter 2: Literature Review

Marine icing problems pose a significant risk to both marine vessel stability and human safety during harsh weather operations. It is important to understand the physics of marine icing phenomena. Most of the present technologies being developed are used to predict icing for freshwater environments and are being used for land based and aeronautical structures. A new or existing technology is required to predict icing conditions and ice growth level to assist the industries for developing anti-icing and de-icing techniques.

Icing can occur at temperatures below freezing when cold water droplets impinge and freeze on unprotected areas that they impact. The rate and amount of ice accretion on an unheated surface depend on the shape, surface finish, size, and speed that the body is traveling, as well as temperature, liquid water concentration and droplet size. Another important aspect for ice accretion is the rate that impinging water will freeze to form ice on a surface. When a forward-facing vessel surface, such as a bow's leading edge passes through wave spray, the impinging droplets can release latent heat and freeze.

Ice accretion is primarily governed by heat transfer from a surface, which includes kinetic heating, convective cooling, evaporative cooling, latent heat of freezing and several smaller contributions from sensible heating and other cooling mechanisms. The primary mechanisms of heat loss are typically convection and evaporation. Convective heat transfer is largely governed by the geometry and speed of the body in water, ice surface roughness

and ambient temperature difference that exists between the surface and local water temperature.

2.1 On-deck icing of marine vessels

This section presents previous research on offshore ice accretion and on-deck icing of marine vessels. Marine icing adversely affects the safety of offshore platforms and small to medium vessels working in arctic and sub-arctic environments. From an analysis performed on ship icing, it was determined that the largest icing rates are in the presence of collision generated sea spray (Zakrzewski, 1987). A better predictive tool to determine the likely locations for ice growth can be obtained from examining the water delivery to an offshore marine structure resulting from spray flux produced by ship-wave impact (Dehghani et al., 2016; Bodaghkhani et al., 2016; Zakrzewski, 1987). Sea spray is transient and stochastic, thus the time dependence and random ice nucleation process cannot be neglected in theoretical approximations (Dehghani et al., 2016; Bodaghkhani et al., 2016; Horjen, 2015). Significant opportunities exist to improve the predictive models for marine icing, especially compared to atmospheric icing (Gent et al. 2000), which typically can be predicted by homogeneous freezing conditions (TO and Wood, 2015).

The surrounding environment, unique structures, and operations of offshore oil platforms make icing a threat to the safety and operational effectiveness of these superstructures. The observation from past incident shows that sea spray icing poses the highest threat to offshore superstructures and is considered as a safety threat for offshore platforms (Ryerson, 2011). Manual de-icing using shovels and mallets is the traditional

way to solve to problem. But various numerical models have been generated over the years to predict icing norms and extremes for offshore structures. RIGICE is a popular numerical tool in this field and has shown good agreement with field data (Forest et al., 2005).

2.2 Water sheets and spray generation on marine vessels

A water sheet layer is generated by a wave impact on a ship bow or offshore structure. As illustrated in Fig. 2.1, water sheet breakup can be experimentally created with customized or commercial flat fan nozzle to investigate the physics of droplet formation from a high energy water jet impacting a deflector surface.
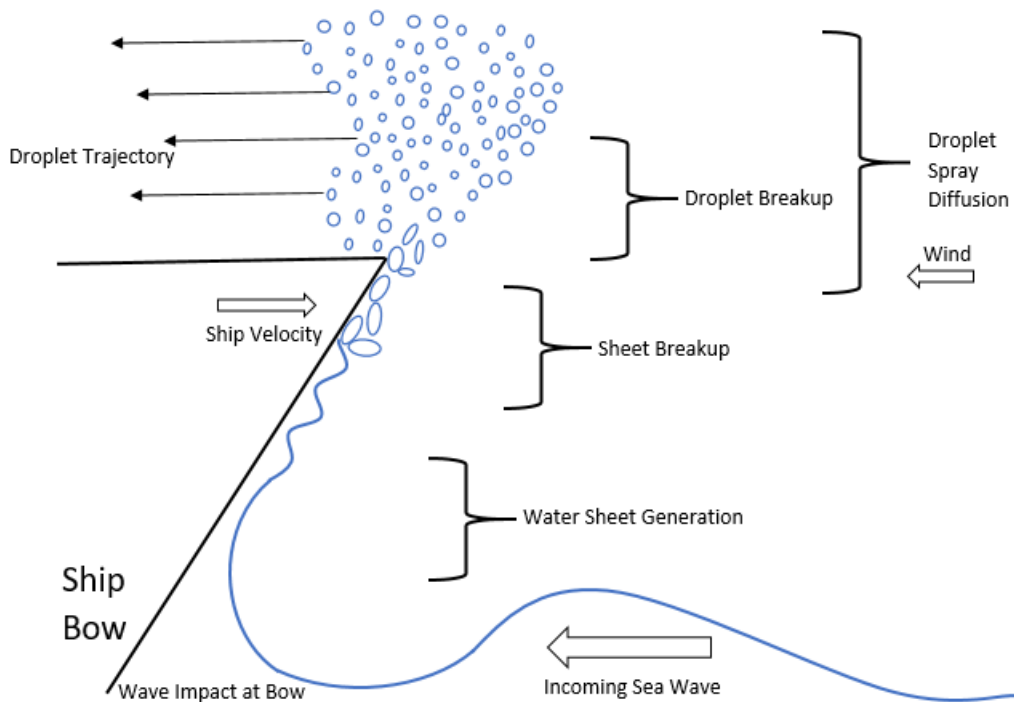
Figure 2.1: A typical wave impact and breakup stages.

Experimental investigation of sheet breakup from impinging jets on a deflector provide the dependence of free jet length and jet Weber number on sheet atomization (Ren and Marshall, 2014). The disintegration of a liquid sheet in the atmosphere is controlled by nozzle shape, spray pressure difference, critical gas-to-liquid density, and viscosity ratios (Negeed et al., 2011; Palacios et al., 2009).

Impacting jet experiments rather than sheets show that the jet velocity profile also dictates the resulting drop diameter and velocity. It has been determined that a shock wave is generated as liquid-jet impacts a solid surface, which causes an appreciable pressure differential at the target surface (Obara et al., 1995). Pressure distribution on marine vessels caused by the impact of incoming water mass on free falling wedge, vertical to slightly inclined wall and model vessels are related to structural integrity and performance of vessels (Yettou et al., 2006; Bullock et al., 2007; Hong et al., 2014). Thus, simplified approaches providing a robust design assessment tool for wave impact has been developing in this field (Hellan et al., 2001). Vessel hull cavitation is a major effect of short water wave pulse, which can significantly change the pressure loading on a hull (Galiev and Flay, 2014).

High-speed visualization is used to observe the stages of a wave impacting a surface. High-speed shadowgraphy is a very useful and precise technique in the field of fluid dynamics (Thoroddsen et al., 2008). Various experimental studies on liquid sheet breakup use this technique in the form of backlight illumination or shadowgraphy (Wahono et al., 2008; Negeed et al., 2011; Obara et al., 1995). This technique has the advantage of

capturing most of the light from the source and is useful for high-speed imaging (Castrejón-Pita et al., 2013).

Spray generation after impact can significantly increase ice accretion rates (Aalbers and Poen, 2015). The wave impact on a ship surface can be divided into a four-step physical process, including (i) spray sheet and jet formation, (ii) strong free surface turbulence interaction, (iii) air entrapment and bubble generation, and (iv) post breaking turbulence and dissipation (Weymouth et al., 2007). It is difficult to develop a numerical model robust enough to predict the formation and flow separation of spray from impacting a solid surface (Gu et al., 2014). Various numerical strategies have been developed that involve using hybrid solver techniques to deal with the non-linearity in ship-wave interaction. Although these long-term developments have shown qualitative similarities in pressure maps for different types of wave impacts, more physics needs to be represented in the numerical models to achieve quantitative consistency (Guilcher et al., 2014).

2.3 Solidification of droplets after striking a super-cooled surface

The secondary object of this research is focused on the experimental measurement of temperature distribution and physical spreading of salt and fresh water droplets on a super-cooled surface. Limited field simulations and experimental investigations have been conducted to understand the physics behind sea spray freezing in terms of several significant parameters (Kulyakhtin et al., 2013; Ozeki et al., 2005; Fukusako et al., 1989). Wind velocity, wind temperature, droplet size, droplet temperature and droplet mass flow rate were considered for the study of Fukusako et al. (1989). The study concluded that ice

accumulation is closely related to mass flow rate of seawater droplets and super cooling of seawater is affected by salt concentration distribution in the ice layer. Also, a dry or wet condition of the impacted solid surface strongly affected the solidification process.

Most previous research focuses on the behaviour of freezing fresh water droplets at impact on different surfaces with ranging wettability, as well as the effect of low temperature environment on airborne water droplets (Prodi et al., 1982; Strub et al., 2003; Fumoto and Kawanami, 2012; Yang et al., 2011; Jung et al., 2012; Jin et al., 2014; Chuah et al., 2016). The phase change from super-cooled liquid to solid is affected by heat and mass transfer (Strub et al., 2003). Such a rapidly evolving event, the phase-by-phase transformation of a cooling droplet, needs high-speed photography (Yang et al., 2011). Salinity significantly affects ice strength (Makkonen, 2012) and salt entrapment, as well as salinity dynamics further affect ice accretion processes (Kulyakhtin et al., 2013). The study by Fukusako et al. (1989) provides an extensive investigation on marine icing in a cold airstream and concludes salt concentration in seawater spray to be significant on the degree of supercooling of saline droplets.

In the last two decades, several numerical models have been developed that focused on the temperature transition of freezing fresh droplets, ice and water growth with the presence of incoming water droplets. If sea water droplets were considered instead of fresh water, the models would need a modified approach to represent entrapped salt movement that controls ice growth in marine conditions (Hindmarsh et al., 2003; Myers and Hammond, 1999; Brakel et al., 2007; Horjen, 2015). An extensive numerical work on sea

spray icing is the two-dimensional icing model of ICEMOD2, which presents a structured model for sea spray icing but cannot fully predict the stochastic spray impingement in field conditions (Horjen, 2015).

Studying heat transfer processes in ice accretion is a challenge in spray icing due to the dynamic fluctuation of temperature at the icing surface. Infrared cameras have been a successful tool for thermal investigation in water and ice (Horjen, 2015; Karev et al., 2007), as well as for non-invasive surface temperature measurement of asymmetric ice growth in an ice wind tunnel. When using IR tools for measurement, the small difference between the emissivity of water and thin bare ice needs to be considered for sub-zero temperatures.

2.4 Summary

To predict ice accretion, water sheet breakup behavior onto a surface needs to be studied closely. In a marine environment, salt water freezing is a common occurrence, thus a comparative study to analyze the difference and similarity between fresh and salt water freezing is an important factor that is not fully understood. This thesis presents the organization of and results from two arrangements of tests covering two aspects of the marine icing process. Despite the fact that the experiments are parts of a larger process, they are completely individual processes and are depicted independently as far as approach, experimental assembly and results. This thesis investigates the two processes in terms of experimental approach and studies them in isolation to better understand the fundamentals of a complicated problem.

Chapter 3: Experimental Design

The main goals of the experiment setups are to investigate (i) water sheet breakup and (ii) water droplet freezing. In the first experiment, water sheet breakup is created by a jet of water hitting a vertical surface. A customized nozzle with a rectangular opening provides the water jet to create water sheet on the target surface upon collision. The detail features of a generated water sheet such as width, height and sheet area are resolved with high-speed visualization. Flow control devices such as butterfly valve, flow regulating valves and flow meters are required to ensure jet speed from in the tests.

In the second experiment, several droplet sizes for solidification are created from different needle sizes mounted on a syringe pump. The syringe pump can control the flow rate to produce 1 to 2 drops per minute. For marine icing situations, a few seconds of cooling is needed to properly represent the physical process. The distance between the cold plate and origin of droplets is varied to investigate the effect of falling height on the freezing behavior. IR technology is used to examine the freezing of water droplet when impacting a flat surface and then the spreading and freezing process that follows impact. Temperature distribution and splash area are physically relevant and measurable variables that show the physical variation during the impact and freezing process of a water droplet.

3.1 Experimental design to study fluid impact and breakup

The schematic in Figure 3.1 shows the components of the fluid impact and breakup setup. The adjustable nozzle is made from pressing part of a circular tube to a 7.7 cm flat section. The flat section of the nozzle has an outer width of 6 cm and can provide a flat jet

of water from its outlet. The vertical surface used as a target surface is a 1 m × 1 m rectangle aluminum plate.

The surface is coated black to obtain a better contrast with the water sheet. The nozzle's angle of attack on the vertical surface is adjustable to the requirement of the test. An arrangement of gate valve, flow control valve and flow meter is added before the nozzle to control the jet speed. The flow meter has an accuracy of ± 3%. The front of the vertical surface is lit with 2500 lumen LED panels. Full resolution of 1280 × 800 is used for the camera recordings to obtain a larger view area. All the video recordings are conducted at 1500 fps. The high-speed camera is focused at the water sheet plane. Both front and side view of each test .1are recorded to obtain details on water sheet height, width, and area.

Table 3.1 presents the experimental variables and their steps. The variable θ denotes the adjustable angle on the nozzle. The jet velocity, V, is varied within the range of 2.4 to 8 m/s. The obtained results for varying θ and V will be analyzed in terms of the height, width, and area of water sheets.

Table 3.1- Experimental plan

Variable	Unit	Range and steps				
θ	°	0	10	20		
V	m/s	2.4	3.2	4.8	6.4	8
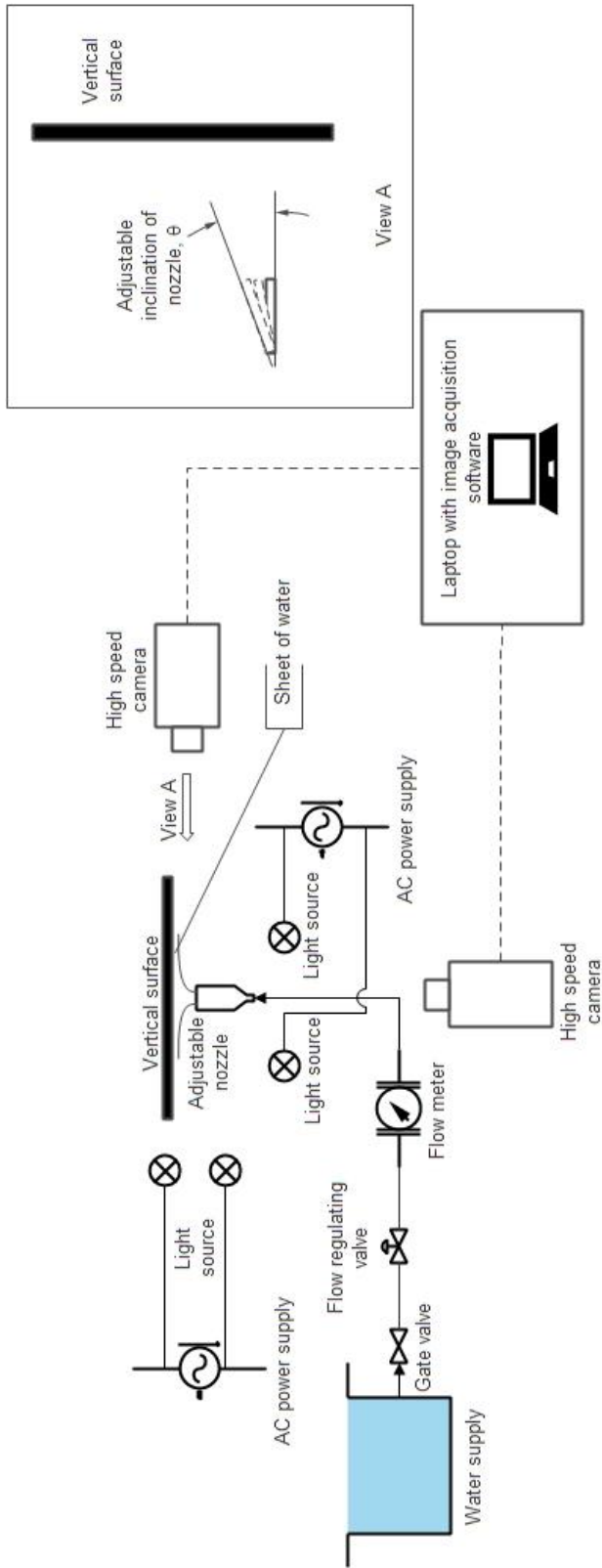
Figure 3.1: Schematic of the experimental setup. View A is shown in the block.

The major components of the fluid impact and breakup setup are:

- water enclosure and the target surface

- water sheet generation system

- flow control system

- High-speed camera and image acquisition system

The water enclosure is a 3 m $\times$ 2 m rectangular water tank fabricated to enclose and drain the huge amount of water generated during the sheet breakup experiment. The simple design and use of thin aluminium sheets allow easy fabrication of the enclosure in sections and then weld and bend the tank per setup requirements. The six legs of the tank enclosure are made mobile with lock wheels to move the setup.
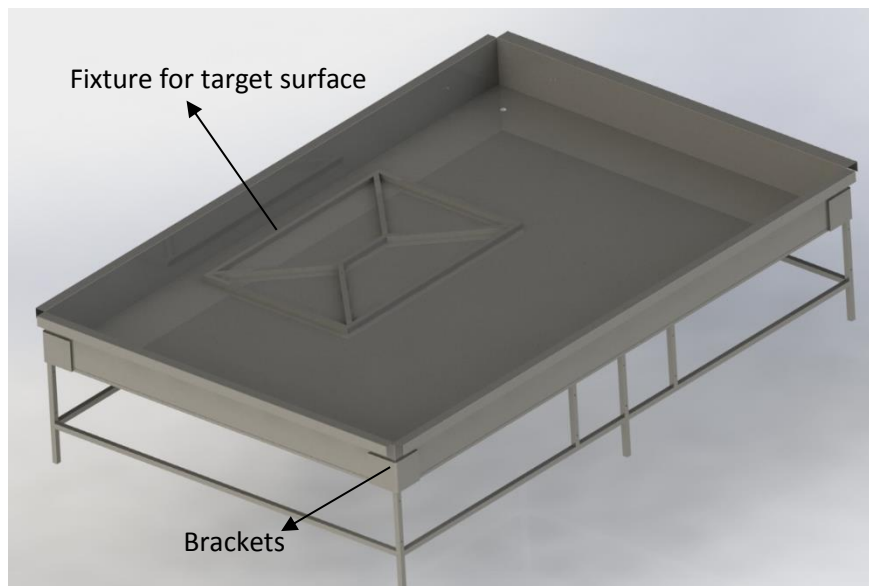
Figure 3.2: CAD drawing of the water enclosure with a fixture for target surface.

Aluminium is selected for the construction material due to its overall light weight, longevity and corrosion resistance from its constant interaction with water. The tank base skeleton is made up of 12.7 mm (width) × 10 mm (height) rectangular tubes with brackets at four corners to hold the tank in position during experiments. The legs and other parts of the tank base are composed of 25.4 mm × 25.4 mm square hollow sections (6.35 mm wall thickness). The CAD drawing in Fig. 3.3 shows the legs, brackets and base of the tank as fabricated in the setup. The water enclosure is bolted with the fixture and base using gaskets to seal the joints from water leakage during the experiments.
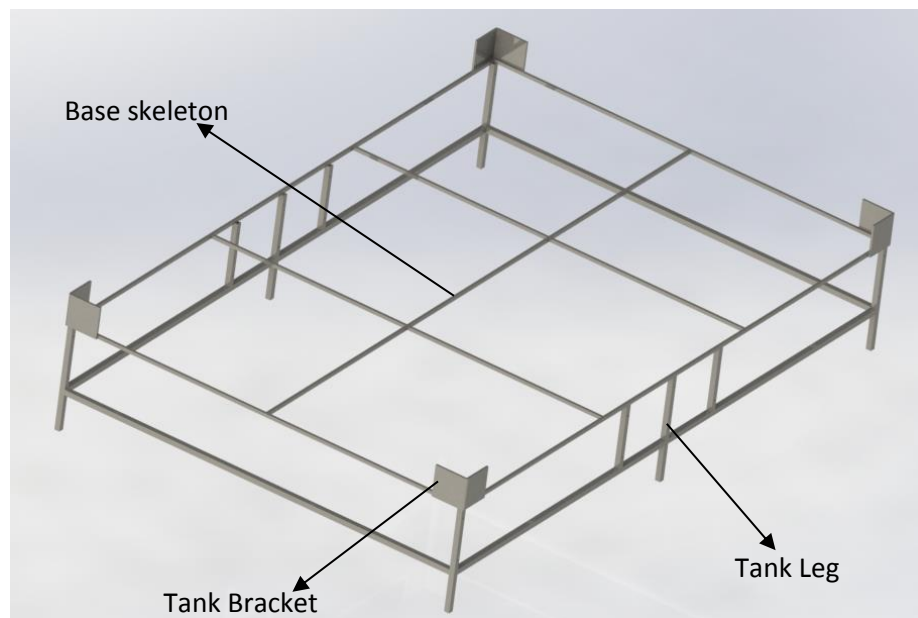
Figure 3.3: CAD drawing of the tank base

The target surface is constructed from 6.35 mm thick aluminium sheet into a "V" shape test section. Each side of the target surface has a 1 m × 1 m flat surface. The specific bend in the construction is aimed at using both the "V" bend and flat surface in front of the

flat-water sheet for requirements of the experiments. The wooden wedges (Fig. 3.4) represent the adjustable inclination possible to the target surface. The inclination is incorporated to investigate the effect of the inclined target against a water sheet breakup. The inclination is performed with 5 bolt threads attached to the water tank through the fixture. A short thread at the tip of the "V" and 4 other along the two sides are used to create inclination in the test. The test object has a water resistant black coating to create a contrast between the sheet breakup and highly reflective aluminium surface during high-speed imaging. The back of the target surface is supported by 25.4 mm $\times$ 25.4 mm square tubes to strengthen the thin aluminium sheet metal against high-velocity water jet generated from the nozzle outlet (Fig. 3.5).
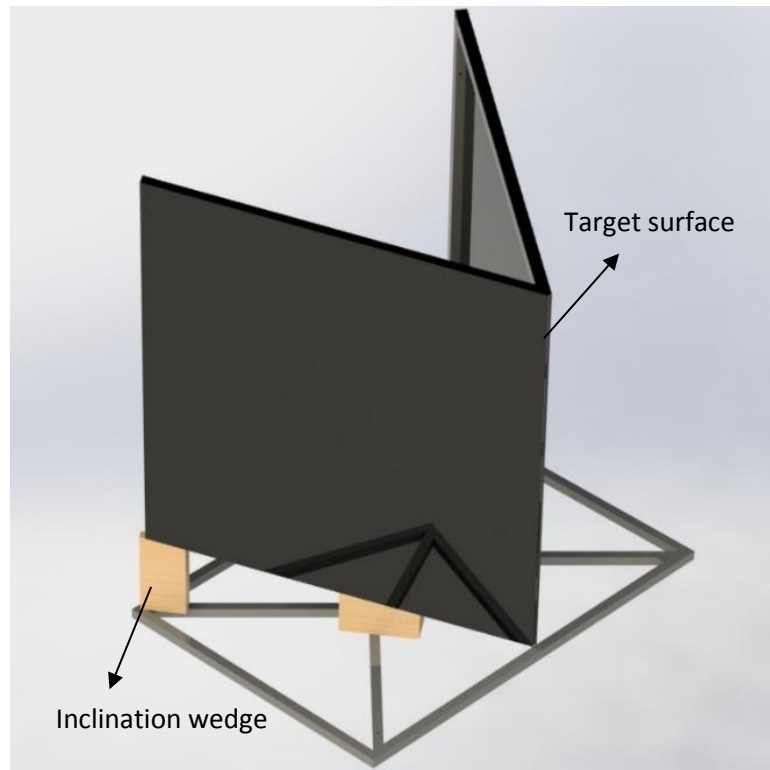
Figure 3.4: Target surface on adjustable inclination-wedge and tank fixture.
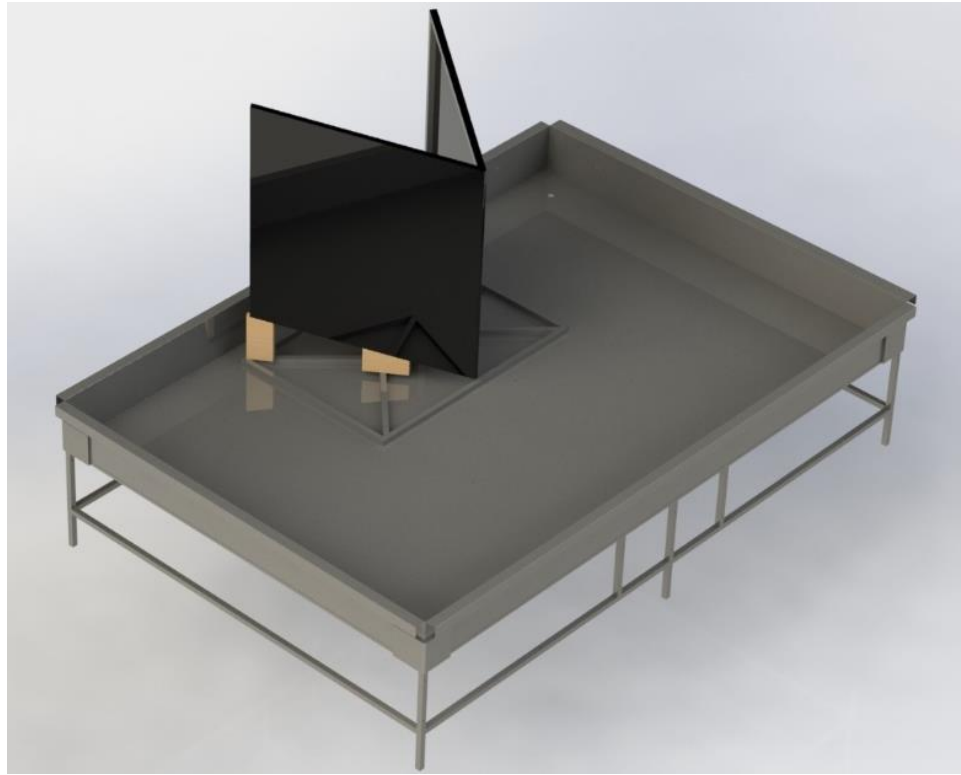
Figure 3.5: CAD drawing of the target surface and water enclosure assembly.

A water sheet is introduced into the setup using a customized nozzle positioned downstream of a water supply system. The support mechanism of the nozzle is fabricated to enable orientation in both horizontal and vertical directions, as well as allow configuration and distance from the test section to be easily altered and customized depending on the test requirements. The change in characteristics of water sheet is obtained with a variety of flow rates and changing the inclination of the nozzle. As illustrated in Fig. 3.6, a circular pipe of 38.1 mm diameter is machine pressed to a 7.7 cm flat and 6 cm wide section that can generate a flat jet of water from its outlet.
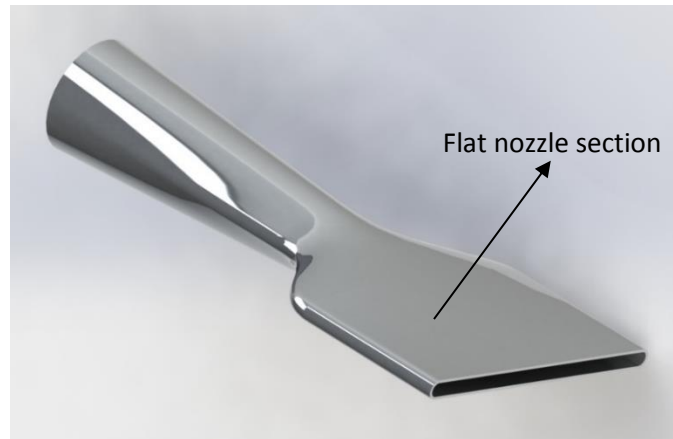
Figure 3.6: CAD drawing of customized flat nozzle, machine pressed from a circular

Stainless steel tube.
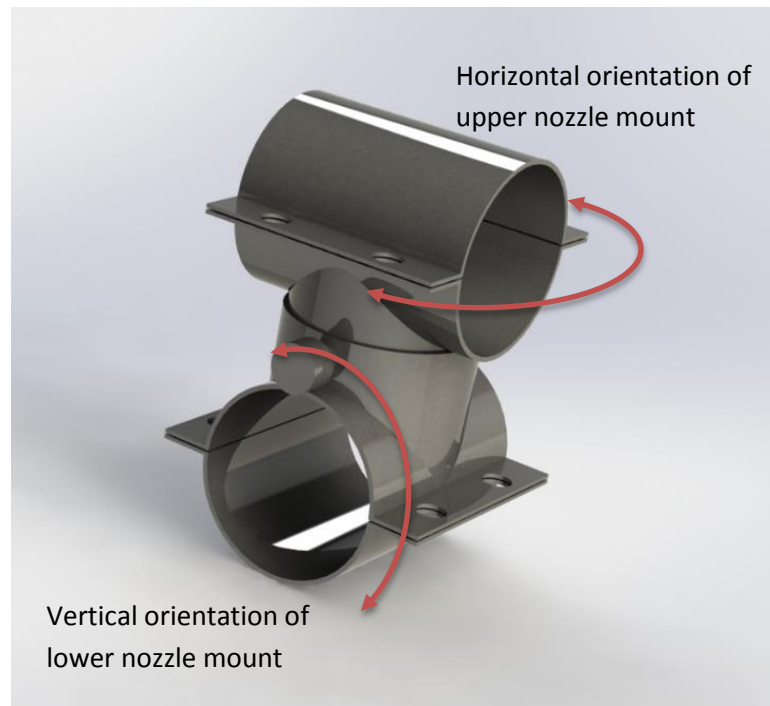
Figure 3.7: CAD drawing of customized nozzle mount, allowing vertical and horizontal

orientation of the nozzle.
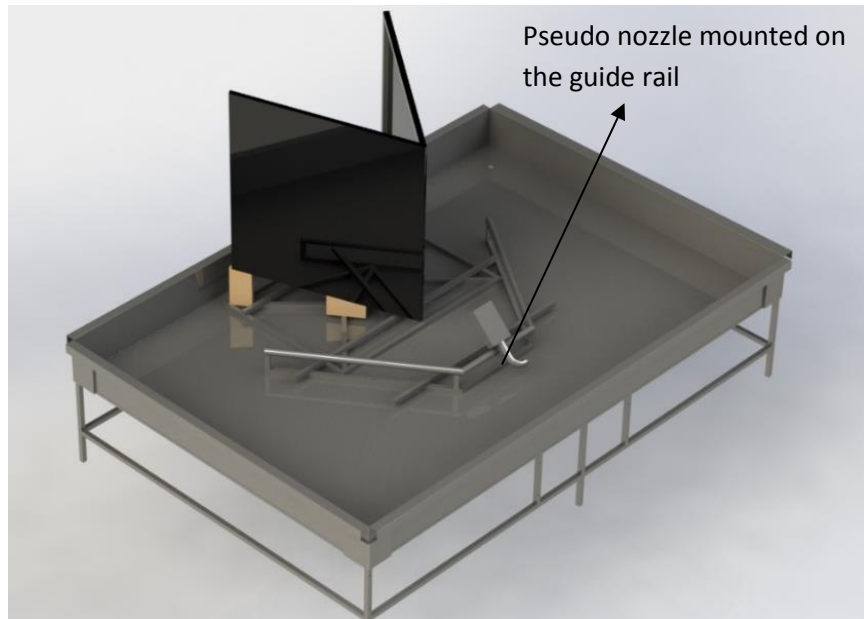
Figure 3.8: Fluid impact and breakup setup with nozzle mount targeted at the test subject.

The machine pressed nozzle is mounted on a customized nozzle holder (Fig. 3.7). The upper portion of the nozzle mount holds the circular section of the nozzle and allows horizontal orientation if required. The lower portion of the nozzle is mounted on a guide railing around the "V" shaped target surface and helps to incline the nozzle at various angles. The overall configuration with the pseudo nozzle with the mount is illustrated in Fig. 3.8. The nozzle can be moved along the guide railing and is mounted on the right side of the railing to use a vertical target surface during the experiments, as shown in Fig. 3.1.

To accurately control the water sheet, a combination of the butterfly valve and flow meter is fitted to the customized nozzle. For most accurate readings, the flowmeter is installed at a minimum distance of at least 10 times the pipe diameter from any fittings. The regular pressure of 50 psi to 60 psi is used in the water supply. The small opening of

the customized nozzle along with the flow control devices result in the desirable range of water sheet velocity in the experiments. The flow control device has a flow range of 15 gpm to 100 gpm, with a ± 3% accuracy. The maximum allowable pressure of water supported by the valve is 175 psi.

The overall event of the sheet breakup on the test object needs full resolution as well as high frame-rate. The widescreen CMOS sensor available in Phantom V611 can capture as high as 6242 frames at full resolution. Additional features include "Extreme Dynamic Range" feature, which gives the ability to obtain two different exposures within a single frame to ensure areas that would otherwise be overexposed, instead contain image detail. Additionally, the auto exposure function lets the camera automatically adjust to changing light conditions. The Phantom (PCC) Camera Control application is used for post processing high-speed capture frame by frame. The software can provide complete creative control over the frames.

3.2 Experimental design to study droplet freezing

A square cold plate of 12.7 cm × 12.7 cm is used in the tests. The cooling bath connected to the cooling plate can maintain temperature stability within ± 0.1°C. The syringe pump connected to the droplet creator has an accuracy of ± 0.5%. A 1:1 ratio of water and ethylene glycol mixture is used as the circulating coolant in the cooling bath. The different droplet sizes are created with a range of needle sizes from 16 to 30 gauge. A 60 ml syringe along with the combination of needle size is referred as the droplet creator in Fig. 3.12.

The long wave IR camera works in the spectral range of 7.5 µm to 13 µm. The IR instrument is calibrated prior to the experiment with a thermocouple for known temperature points. The images obtained from the thermal camera are also calibrated against a known length on the target surface to determine the splash area of the droplet upon impact on the cold plate surface. A salinity meter measures the droplet salinity and has a volume accuracy of ± 0.5%. The instrument is calibrated against a standard solution. The surrounding environment is maintained at 18°C and room temperature water is used in both fresh and salt water experiment.
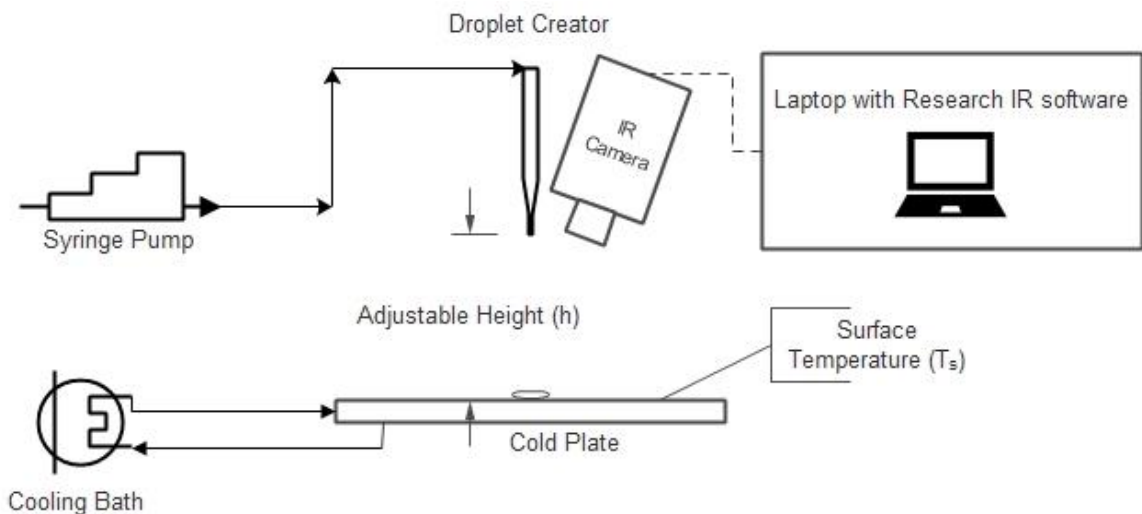
Figure 3.9: Schematic of the experimental setup.

Table 3.2 presents the variable range and steps used for fresh and salt water experiments. The variable T_s represents the surface temperature of the cold plate during the experiments. The temperature of the surface is varied in the range of -5°C to -25°C by circulating the coolant from the cold bath. The diameter of the falling droplets, d, is varied

from 2 to 5 mm. The same flow rate from the syringe pump with different needle sizes helps to create the droplet sizes. The diameter of the droplets is measured with standard grids in high-speed frame capture. The adjustable falling height, h, of the droplets is varied from 10 cm to 130 cm. An individual droplet impact and freezing on a cold surface is studied with the experimental setup.

Table 3.2 - Experimental plan including the target variables and their test steps

Variable and unit	T_s (°C)	d (mm)	h (cm)
	-5	2	10
	-10	3	50
Range and steps	-15	4	90
	-20	5	130
	-25		

The droplet generation system is designed to create droplets of different sizes. A combination of commercially available dispensing needle sizes, PVC tubing and syringe pump is assembled together to achieve the size of droplet required for investigation. A syringe pump is a small infusion pump that can be used to gradually regulate small amounts of fluid. Unit rates ranging from ml/min to µl/hr can be achieved with the pump. The inside diameter of the syringe mounted on the pump can be separately set in millimeters. After a diameter is entered, the required flow rate can be set accordingly. PVC clear tubing allows monitoring of the flow. The cooling system is designed to provide a supercooled surface

with a square cold plate and thermal bath. A customized camera support stand is required to adjust the camera focus in vertical and horizontal positions. As illustrated in Fig. 3.13, a lightweight aluminium support stand and fixture are designed and fabricated for this purpose. The stand is 1.5 m (width) × 2 m (height) overall and the height can be adjusted from 1.5 m to 2 m. A 7.62 cm × 7.62 cm camera fixture (Fig. 3.14) is attached to the horizontal section of the square tube structure. The camera fixture can provide 100° of rotation between horizontal and vertical position. The arc guideways on two sides of the camera fixture provide a smooth transition from horizontal to vertical positions. A pair of guide screws on each side fix the camera at any angle within the guideway.

Figure 3.10: Customized support stand for IR/High-speed camera.
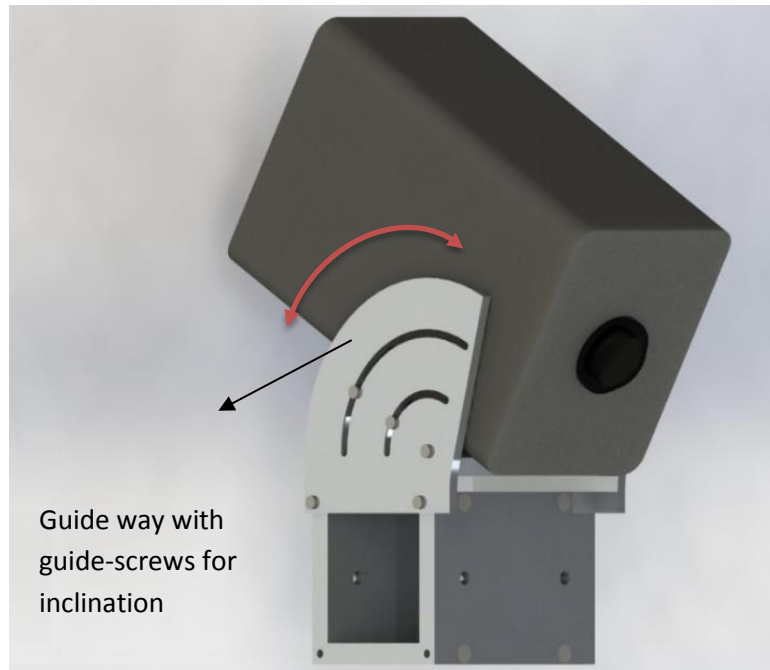
Figure 3.11: Camera fixture with guide screws to provide adjustable inclination.

Chapter 4: Results and Discussion

4.1 Extent of Water Sheet Breakup on a Vertical Surface

4.1.1 Water sheet width and height

In this section, the water sheets are analyzed in terms of width and height. Figure 4.1 shows various types of water sheets at 0° nozzle position. The sequential images from Fig. 4.1 a to e show the change in water sheet size as the jet velocity is increased from 2.4 to 8 m/s. All the sheets cast a triangular shed on the vertical surface. The size of the shed continued to get bigger as the jet velocity is increased. For a low-velocity jet, the generated sheet on the surface does not form any additional droplets from the splash. However, as the jet velocity continues to increase, the sheets are more likely to break up and form droplets. The phenomenon is illustrated in Fig. 4.1 c to e.

Figure 4.1: Variation of water sheet width (W) on a vertical surface at θ = 0° and V for (a) 2.4 m/s, (b) 3.2 m/s, (c) 4.8 m/s, (d) 6.4 m/s, and (e) 8 m/s.

Figure 4.2 illustrates the variation of water sheet width, W, at various jet velocities, V, and inclinations, θ, of the nozzle. The plots show a positive effect of velocity on sheet

width. The width varies from 2.61 to 4.75 cm for different θ. The standard deviation of the

measured data is also presented in the plots as error bars.

Figure 4.2: Variation of water sheet width (W) for resulting fluid impact on a vertical

surface ($\theta = 0° \sim 20°$, V = 2.4 to 8 m/s).

Figure 4.3 shows the side view of the setup, which is used to measure the height of

the generated sheet at the same θ and V. The entire sheet cannot be focused simultaneously

on the fixed lens, therefore, a portion of the image is blurrier than others. The height, H,

denotes the rise of water sheet above the nozzle tip. The generated spray from the water

sheet is excluded because they cause uncertainty in the measurement height. The sequential

side captures in Fig. 4.3 also show the increased quantity of spray obtained at a higher

velocity than the front captures in Fig. 4.1.

The images are calibrated against a known length in the same plane of the sheet prior to the tests. But sprays are not included in the measurement process because of the randomness of the sprays generated on such a large scale. The measurements are limited to the macroscopic dimension of width, height, and area. The physical behavior of the water sheet at different θ of the nozzle is investigated. The water sheet shows an inclination towards falling back on the nozzle at θ = 0°. Thus, almost all the sheet and generated spray tends to remain on the right side of the image rather than projecting some part of the sheet beyond the vertical surface.

Figure 4.3: Variation of water sheet height (H) at θ = 0° and V for (a) 2.4 m/s, (b) 3.2 m/s, (c) 4.8 m/s, (d) 6.4 m/s, and (e) 8 m/s.

A parameter, W*, represents the dimensionless width for the water sheet profiles. The variable W* is the ratio of a sheet width and average sheet width for the same test. Each data point presented in the plot has five consecutive trial data points to show the

deviation of the test measurements. Figure 4.4 shows a slow growth of W* for different jet velocities. All the plots show reluctant growth with the increase in θ. The variation of W* in the plots range from as low as 0.03 to a maximum of 0.13. The minor variation of the dimensionless parameter suggests the minute effect of θ on W*.
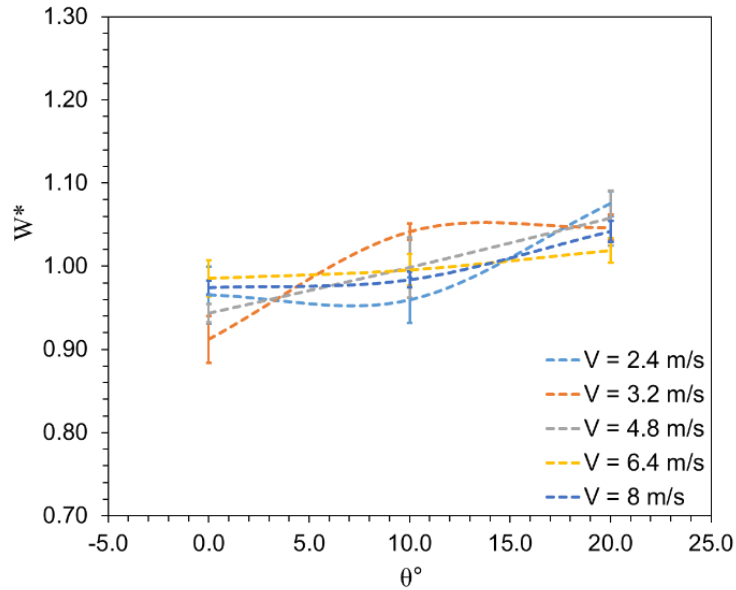
Figure 4.4: Variation of dimensionless width (W*) upon impact on a vertical surface (θ = 0° ~ 20°, V = 2.4 to 8 m/s).

Fig. 4.5 presents the variation of water sheet height for the same variable set of θ and V. There is a clear indication of the rise of sheet height for increasing jet velocities when θ is maintained constant. However, a clear trend for increasing θ cannot be expressed from the plots. The difference between the data plots for different θ is also not consistent and vary in the range of 1.7 to 14.9 cm. It strengthens the concept of V being a stronger factor than θ in terms of affecting the sheet height in the test. The standard deviation of the measured data points is presented as error bar and varies from 0.46 to 6.54 cm.
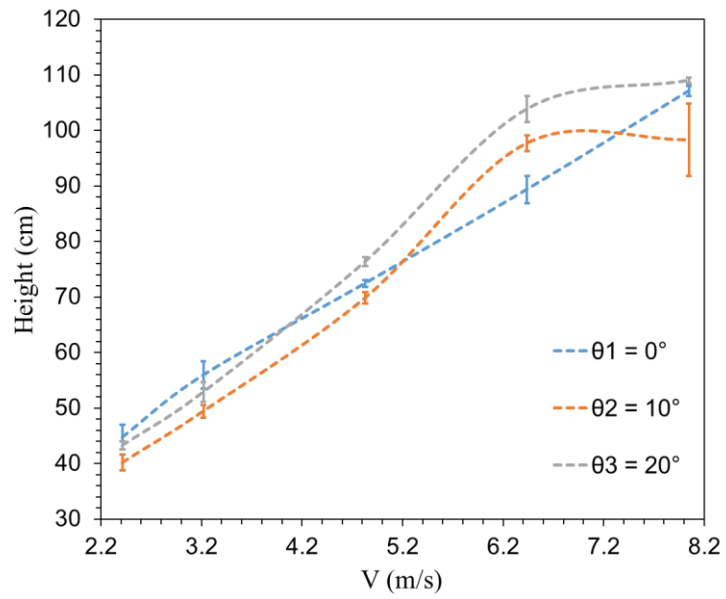
Figure 4.5: Variation of water sheet height (H) for resulting fluid impact on a vertical surface ($\theta = 0° \sim 20°$, V = 2.4 to 8 m/s).
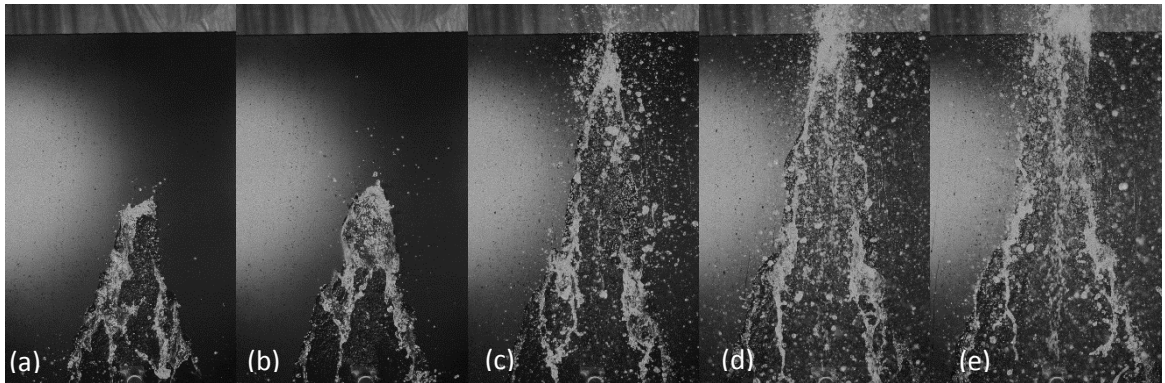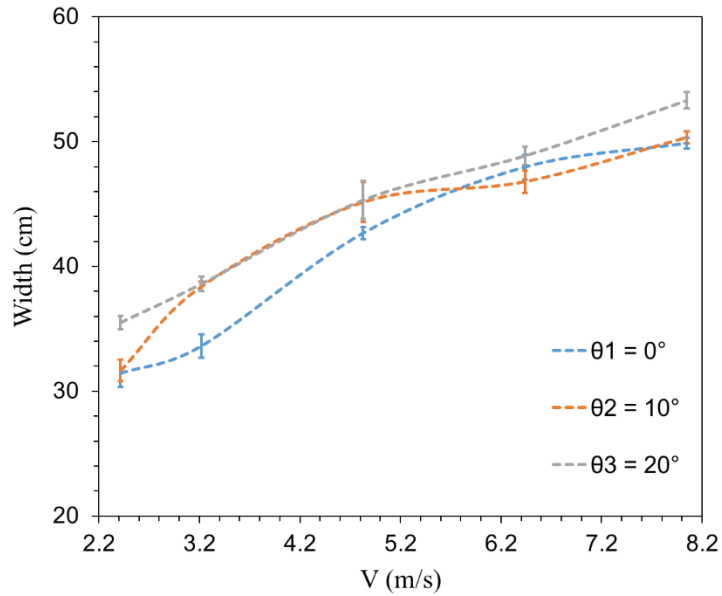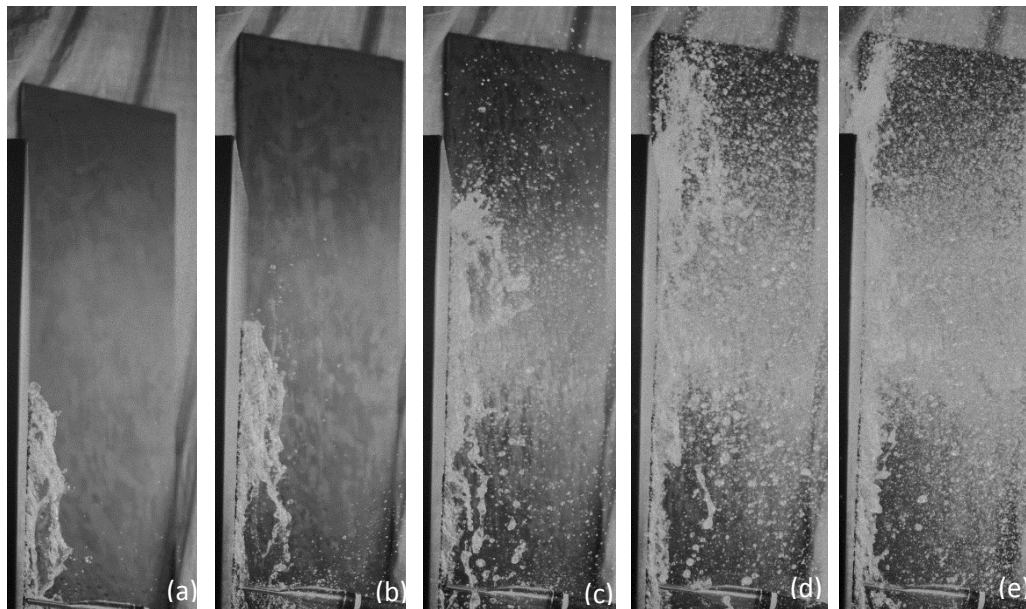

Figure 4.6: Variation of water sheet height (H) at $\theta = 10°$ and V for (a) 2.4 m/s, (b) 3.2 m/s, (c) 4.8 m/s, (d) 6.4 m/s, and (e) 8 m/s.

As illustrated in Fig. 4.6, the water sheets formed at θ = 10° rise straight along the face of the vertical surface and show a tendency to shed some water beyond the vertical face. This phenomenon is much more significant and visible at a higher jet velocities, such as 6.8 m/s and 8 m/s. The corresponding images are shown from Fig. 4.6 d to e. At higher velocities, the sheets have enough energy to cross the height barrier of the surface and deliver water beyond the vertical margin to the left.
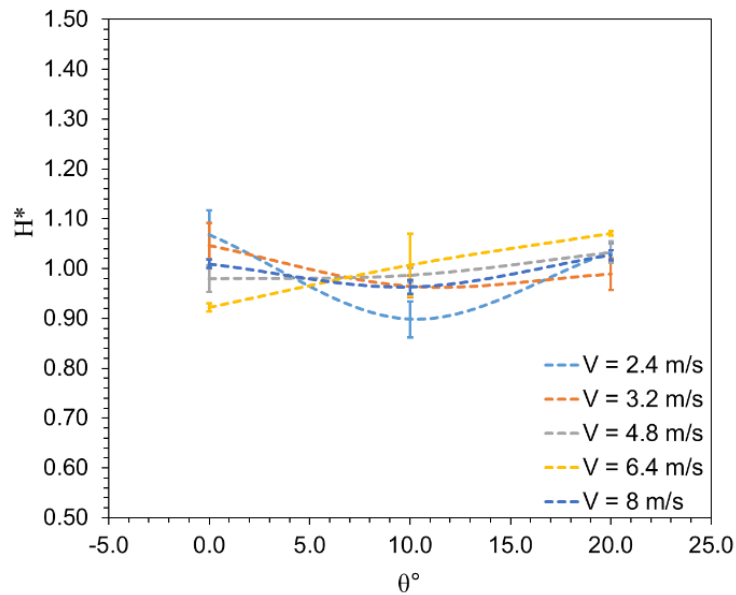
Figure 4.7: Variation of dimensionless height (H*) upon impact on a vertical surface (θ = 0° ~ 20°, V = 2.4 to 8 m/s).

As illustrated in Fig 4.7, a dimensionless height parameter, H*, shows the significance of θ on the sheet height. The behavior of the plots suggests that the angle of attack has little or no effect on the variable H*. The dimensionless parameter is a ratio of a sheet height to the average value of the data set obtained for the same test. A small increase in H* is noticeable from 6.4 m/s to 8 m/s, however, the behavior is random at lower

velocities. Therefore, the change in θ can be considered insignificant with the variation of H*.

The effect of water shedding beyond the vertical surface increases significantly with θ. Figure 4.8 shows that at θ = 20°, the sheet continues to incline more onto the surface upon impact from the jet. At V = 6.4 m/s and above, the sheets rise beyond the vertical margin and shed more water to the left. The sequential side captures for Figs. 4.3, 4.6 and 4.8 show that θ is more important for factors such as water shedding beyond the target surface than other variables discussed in this section.
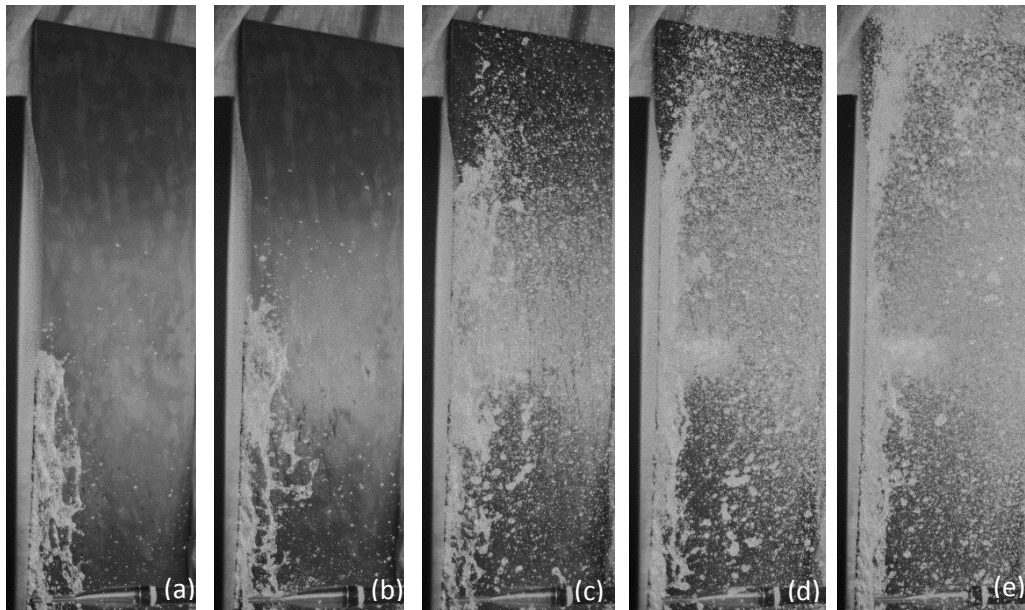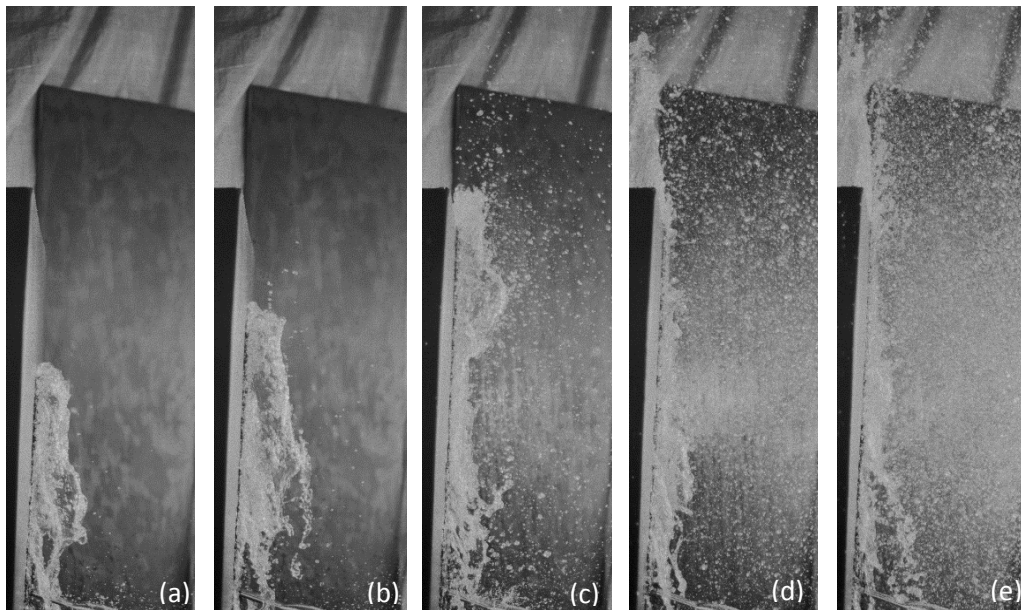

Figure 4.8: Variation of water sheet height (H) at θ = 20° and V for (a) 2.4 m/s, (b) 3.2 m/s, (c) 4.8 m/s, (d) 6.4 m/s, and (e) 8 m/s.

Experimental data plots and images show that the height and width of a water sheet are affected mostly by jet velocity. The adjustable attack angle of the nozzle contributes

more to the water shedding of the sheet beyond the vertical surface and thus provides a concept of water trajectory during sheet splash.

4.1.2 Water sheet area

Another possible feature to define the sheet behavior is identified as the area shaded by sheet splash on the surface. The water sheet, produced from the jet-surface collision, went both up and down the surface. In the measurements, only the shaded area above the nozzle tip is considered as the water sheet area, A. Figure 4.9 shows the change in water sheet area as the jet velocity continues to increase, at $\theta = 10°$.

Figure 4.9: Change in water sheet area (A) on a vertical surface at $\theta = 10°$ and V for (a) 2.4 m/s, (b) 3.2 m/s, (c) 4.8 m/s, (d) 6.4 m/s, and (e) 8 m/s.

Figure 4.10 shows the plots of A at θ from 0° to 20°. The figure shows that at a certain attack angle, as the jet velocity continues the increase the sheet area also increases in a linear manner. The flatness of the plots at the highest velocity (8 m/s) might have been caused by the measuring difficulty of the sheet area. Figs. 4.1e, 4.9e and 4.11e also show the corresponding sheet area forming more spray at the tip of the sheet and dispersing the

overall appearance of the sheet. The plots suggest a rapid change of sheet area between θ_1 = 0° and θ_2 = 10°. In comparison, the change of water sheet area in between the plots of θ_2 = 10° and θ_3 = 20° is negligible.
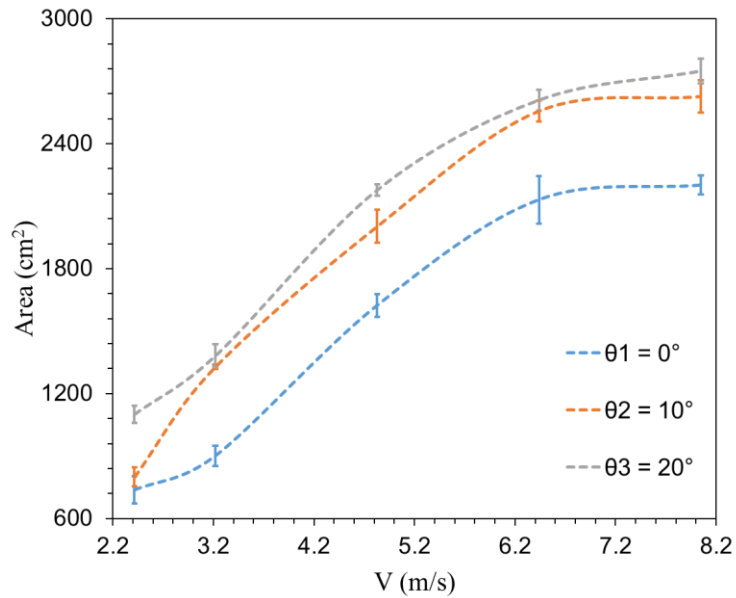

Figure 4.10: Change in water sheet area (A) for resulting fluid impact on a vertical surface (θ = 0°~20°, V = 2.4 to 8 m/s).

Figure 4.11 shows the change in A for increasing jet velocity, at θ = 20°. The images from Fig. 4.1 suggest that at 0° inclination of the nozzle, the tip of the water sheet area is very unstable and at higher velocities, the tip is dispersed into sprays very early. As θ increase from 10° to 20° (Figs. 4.9 and 4.11) the tip of the sheet area shows more stability and remains sharp, even at high jet velocities. The side view of Figs. 4.6 and 4.8 illustrate that at V ≥ 6.4 m/s the formed sheets have a clear path to shed water beyond the vertical surface and to the other side. Thus, the sheet area appears to be more stable at θ higher than 0°. A dimensionless parameter, A*, defined as the ratio of a sheet area and the average

value of the data set obtained for the same test, is introduced to evaluate the effect of attack

angle on water sheet area.
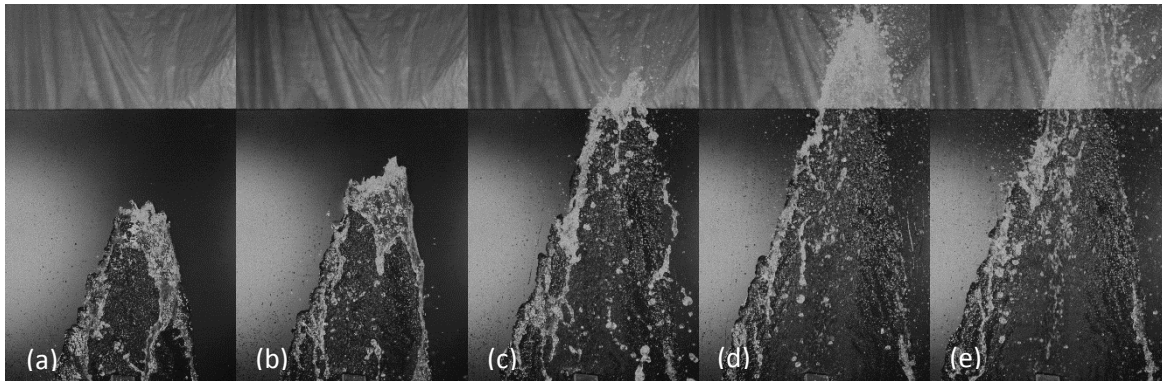
Figure 4.11: Change in water sheet area (A) on a vertical surface at θ = 20° and V for (a)
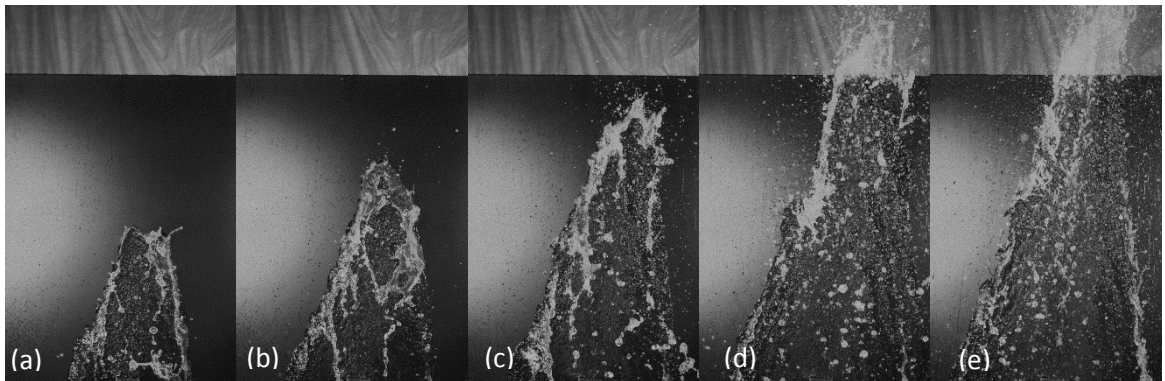
2.4 m/s, (b) 3.2 m/s, (c) 4.8 m/s, (d) 6.4 m/s, and (e) 8 m/s.
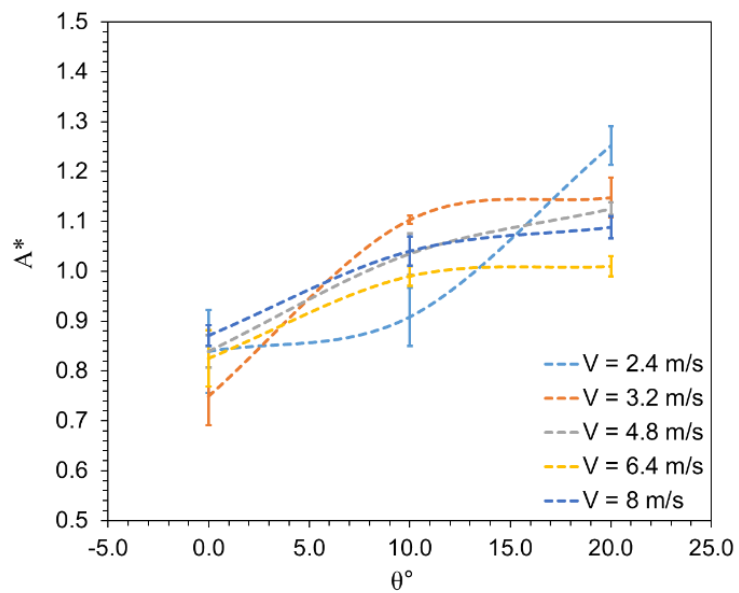
Figure 4.12: Variation of dimensionless area (A*) upon impact on a vertical surface (θ =

0° ~ 20°, V = 2.4 to 8 m/s).

As illustrated in Fig. 4.12, for V > 2.4 m/s the most notable change in A* occurs at 0° to 10°. For V = 2.4 m/s a continuous increase in A* from 0° to 20° is evident. This behavior suggests that low-velocity jet-surface collisions can be affected by higher attack angles and significantly affect A*. As V continues to increase, the significance of θ > 10° on A* is minimized.

4.2 Solidification of Saline and Fresh Water Droplets

4.2.1 Fresh water

In this section, fresh water droplet freezing is analyzed in terms of thermal behavior, phase change, and splash area generated after impact on the surface. During the experiment, the cold plate is placed within the minimum possible focal distance (0.4 m) from the IR camera. The distance between the camera and cold plate is not changed to ensure optimal thermal capture. A customized stand adjusts the distance between the needle and cold surface in the range of 10 cm to 130 cm.

Figure 4.13 shows the plots of maximum surface temperature, T_{max}, obtained from the droplet region of interest (ROI), with time starting at droplet impact (for highest altitude, h = 130 cm). The variable T_{max} provides the maximum temperature for a selected ROI and thus is included in the analysis to understand the end of freezing or close to plate temperature dynamics. All the fresh water droplets cool to surface temperature, T_s, within 0.4 to 0.8 s after the impact. For droplet diameter, d = 5 mm, T_{max} is steady after reaching 0°C and remains steady for 0.3 s more than droplet diameters of 2 to 4 mm. After the short steady region, all the plots follow a rapid decrease in the cold plate temperature. The first

stage of liquid cooling shows a negative slope, the phase change in the form of a flatter slope and finally the last stage of solidification in the form of a longer slope to surface temperature, T_s. Larger droplets take more time to solidify than smaller droplets.
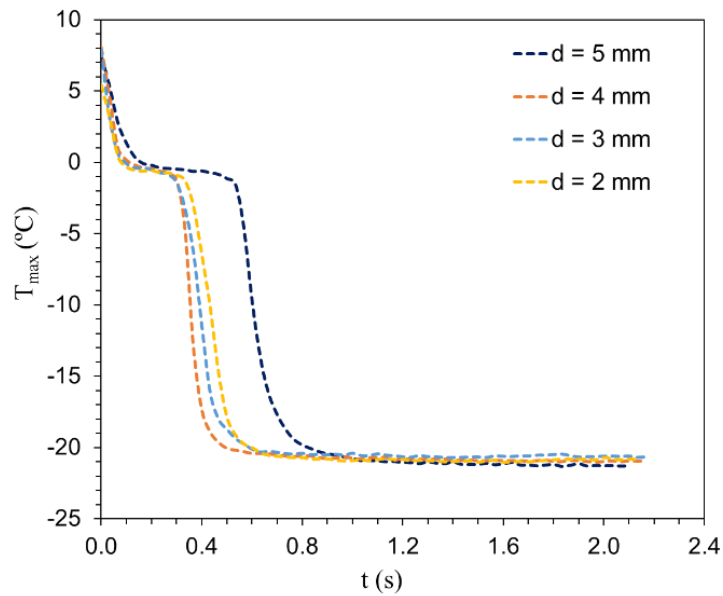
Figure 4.13: Variation of maximum temperature of droplet splash on a cold surface ($T_s =$ -25°C, h = 130 cm).

To maintain consistency, time (t) starts from exactly the same impact frame that creates the maximum splash on the target surface and is equal to zero. The sequential order of images along with their respective time stamp in Fig. 4.14 show the thermal behavior of droplets as they change from yellow-red to blue-violet. Yellow is the maximum temperature for the ROI and violet denotes the coldest zone in the images. In smaller droplets, as shown in Fig. 4.14 a to l, the freezing has started from the periphery of the droplet and from the central impact point denoted by blue or green zones, as seen in Fig. 4.14 f and j. For larger droplets, as shown in Fig. 4.14 m to p, the freezing starts

36

simultaneously at various regions within the droplet but eventually takes much more time for the droplet to reach the surface temperature of the cold plate.
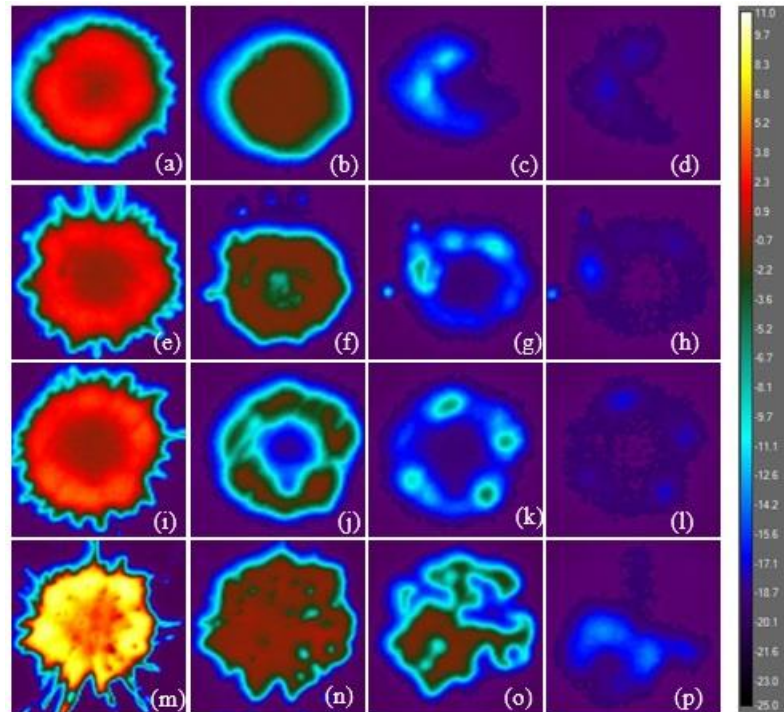
Figure 4.14: Thermal images in sequence for different droplet sizes falling from h = 130 cm (a) d = 2 mm t = 0 s, (b) d = 2 mm t = 0.267 s, (c) d = 2 mm t = 0.467 s, (d) d = 2 mm t = 0.533 s; (e) d = 3 mm t = 0 s, (f)) d = 3 mm t = 0.233 s, (g)) d = 3 mm t = 0.4 s, (h)) d = 3 mm t = 0.467 s; (i)) d = 4 mm t = 0 s, (j) d = 4 mm t = 0.233 s, (k) d = 4 mm t = 0.366 s, (l) d = 4 mm t = 0.433 s; (m) d = 5 mm t = 0 s, (n) d = 5 mm t = 0.233 s, (o) d = 5 mm t = 0.467 s, (p) d = 5 mm t = 0.7 s.

As illustrated in Fig. 4.15, a trend of linear increase of splash area with droplet diameter is evident in the experimental data. As illustrated in Fig. 4.14, when larger droplets fall from 130 cm, they tend to produce tentacles on impact and create a larger splash area.

Compared to d = 2 mm, the splash area shows a 160.9% increase for a 5 mm falling droplet. As surface temperature is maintained fixed at -25°C, the large volume of increasing droplet size influences the splash area. The standard deviation of measured splash area is represented by the error bars and vary from 0.02 to 0.05 cm^2.
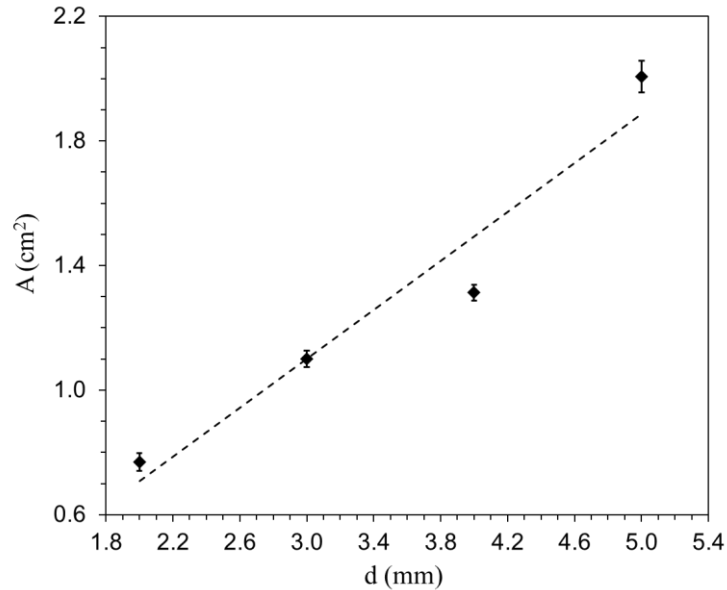
Figure 4.15: Splash area (A) for droplets upon impact on a cold surface at T_s = -25°C and h = 130 cm. Linear regression of the experimental data points is also shown.

4.2.2 Salt water

For changing surface temperature, falling altitude and varying droplet sizes, this section analyze saline water behavior during solidification. Salt water droplets are tested with the same experimental method as presented in Table 3.2 in Chapter 3. To ensure the salinity of the solution, the electrode connected to the salinity meter is rinsed with distilled water, dried and dipped into a standard solution for calibration. A typical marine salinity of

35 ppt is maintained in the experiments. Figure 4.16 shows the test result for the smallest droplet falling from a height of 130 cm with varying surface temperatures from -5°C to -25°C. The plots illustrate the change of average surface temperature obtained from the droplet ROI with time, i.e., T_{mean}. The droplet diameter is 2 mm in the plots. As illustrated in Fig. 4.16, cooling is faster as the surface temperature is reduced. The reduction of surface temperature highly affects the cooling time of the droplet after impact.
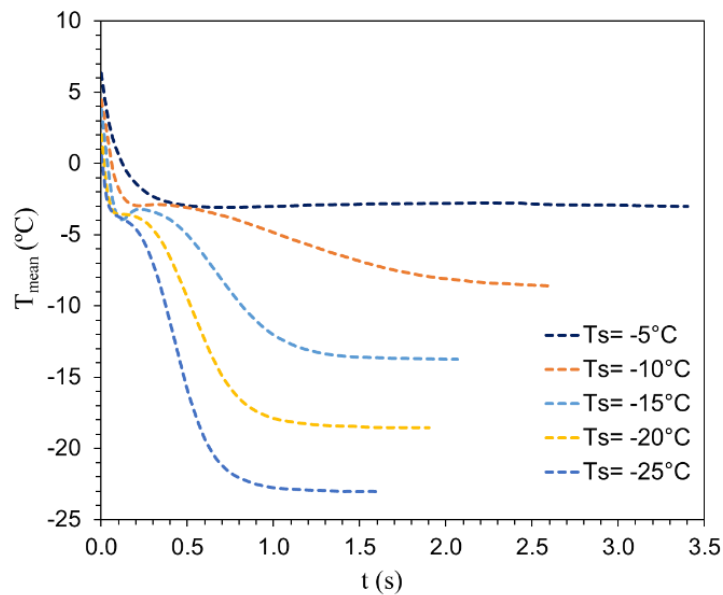
Figure 4.16: Variation of mean temperature for d = 2 mm droplet falling from h = 130 cm at various surface temperature.

Figure 4.17 illustrates the freezing behavior in the form of IR images for the same variable settings as Fig. 4.16, and the sequential images show the freezing morphology of salt water droplets. For a relatively high-temperature thermal image, as shown in Fig. 4.17 i, m and q, the spreading fingers of the droplets are much more visible. However, as the

surface temperature continues to reduce, as shown in Fig. 4.17 a and e, there is less finger spreading.

At higher T_s, such as -5°C to -15°C, the droplets have more time to spread fingers as the phase change process is longer. As the surface temperature continues to decrease, the time for the droplet to spread and solidify is reduced. Therefore, fewer tentacles from the droplet spread are visible at lower T_s. For higher T_s, as illustrated in Fig. 4.17 m to p and q to t, the overall droplet region continues to freeze to surface temperature rather than freezing simultaneously at various zones inside the droplet.

Due to the presence of salt particles in the water droplet, freezing does not occur at various small regions inside the droplet. In salt water freezing, as the droplet continues to cool down to the surface temperature, salt particles are continuously rejected and thus the random nucleation sites observed in fresh water freezing are absent in Figure 4.17. Due to this process, salt water droplets exhibit uniform heat transfer with the cold plate. This behavior is evident in Fig. 4.17 b, f, j, n and r. In the case of fresh water, the growth of several small circular freezing regions was observed inside the droplet splash. The behavior is evident in Fig. 4.14 f, j and n. Eventually, as the temperature of the surface continues to reduce, freezing regions within the droplet center begins to emerge. As the volume of water does not change in Fig. 4.17, with decreasing surface temperature the droplet physically begins to cool faster than usual and we can see the start of solidification from the impact center of the splash. This behavior is prominent in Fig. 4.17 c, g and k.
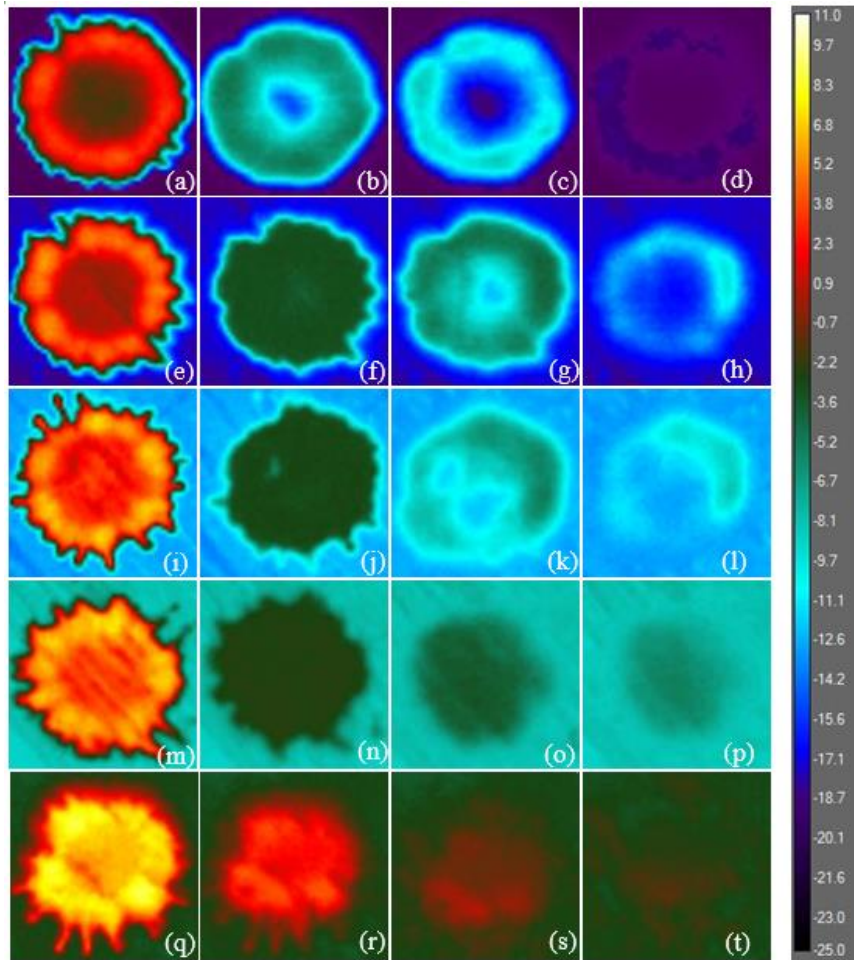
Figure 4.17: Thermal images on impact for d = 2 mm saline droplet falling from h = 130 cm at different surface temperature (a)Ts = -25°C t = 0 s, (b) Ts = -25°C t = 0.4 s, (c) Ts = -25°C t = 0.5 s, (d) Ts = -25°C t = 0.7 s; (e) Ts = -20°C t = 0 s, (f) Ts = -20°C t = 0.267 s, (g) Ts = -20°C t = 0.5 s, (h) Ts = -20°C t = 0.733 s; (i) Ts = -15°C t = 0 s, (j) Ts = -15°C t = 0.333 s, (k) Ts = -15°C t = 0.833 s, (l) Ts = -15°C t = 1.033 s; (m) Ts = -10°C t = 0 s, (n) Ts = -10°C t = 0.434 s, (o) Ts = -10°C t = 1.234 s, (p) Ts = -10°C t = 1.7 s; (q) Ts = -5°C t = 0 s, (r) Ts = -5°C t = 0.1 s (s) Ts = -5°C t = 0.233 s (t) Ts = -5°C t = 0.366 s.
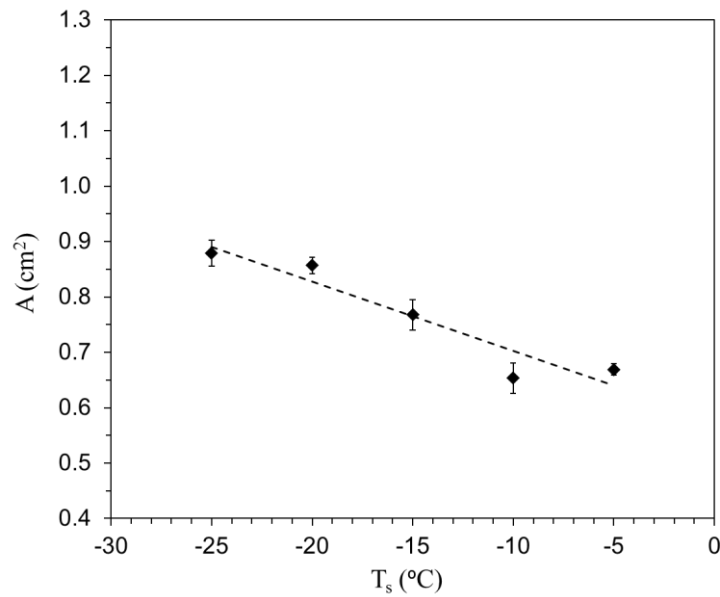
Figure 4.18: Variation of splash area (A) upon impact for d = 2 mm saline droplet falling from h = 130 cm at various surface temperature. Linear regression of the experimental data points is also shown.

Changing surface temperature also has a microscopic effect on the splash area. As illustrated in Fig. 4.18, at lower surface temperature the splash area tends to get larger, even though more splash fingers are visible at higher surface temperatures. As the surface temperature decreases, the splash area upon impact has less time to contract before freezing, which increases the splash area. The error bars for the plot are presented in terms of standard deviation and vary from 0.01 to 0.03 cm^2. The falling height is maintained at 130 cm.

4.2.3 Comparison

In this section, the similarities and key differences between the impact and freezing of fresh and salt water are presented. Fig. 4.19 presents the freezing process of fresh and salt water droplets of the same size and falling altitude. As illustrated by the fresh water images from Fig. 4.19 a to p, the tendency in fresh water freezing is to reduce the periphery of the impact splash area and initiate a central violet solidification region, which is most likely to be the impact center of the droplet.
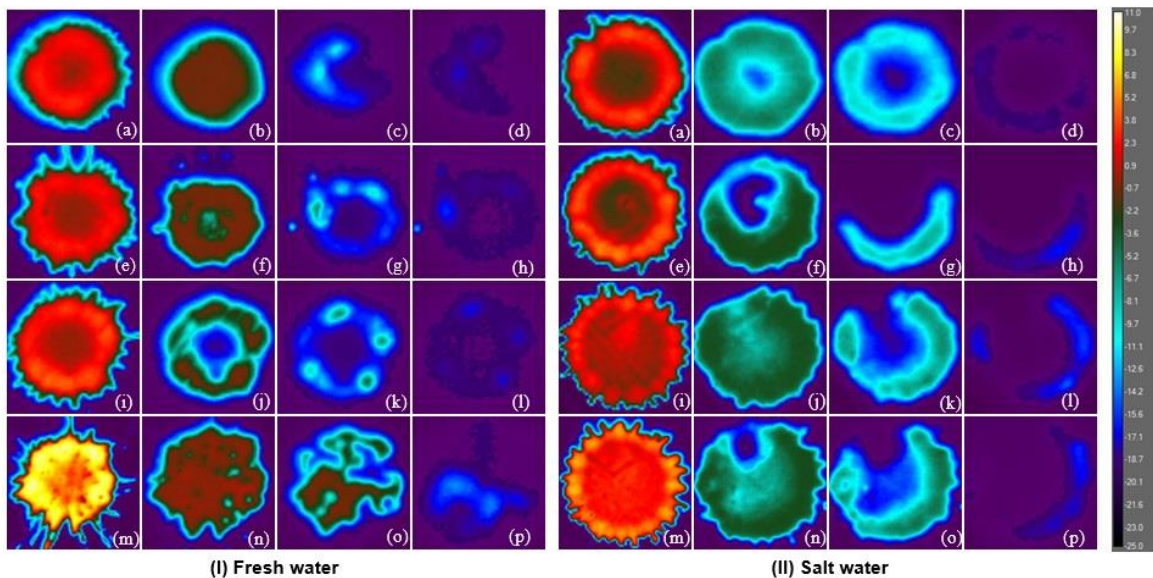
Figure 4.19: Thermal images in sequence for d = 2 mm (a to d), 3 mm (e to h), 4 mm (i to l) and 5 mm (m to p) droplet falling from h = 130 cm (I) Fresh water (II) Salt water.

In salt water freezing, as the droplet contacts the cold surface and begins freezing, there is more uniform heat transfer between the droplet and surface, as seen by the light green zone in the images. A peripheral decrease of the splash area in freshwater freezing is

not evident in the salt water freezing experiments. The growth of an off-centre violet region is again visible in salt water freezing similar to the fresh water experiments.

Figure 4.20 shows the effect of salt particles on splash area with increasing droplet size. The standard deviation for the salt water splash area data varies from 0.05 to 0.07 cm^2. Due to the presence of salt in sea water, the salt water droplets have a higher density than fresh water droplets. As the volume of saline droplets increases, the mass increases by a larger factor. Thus, saline droplets produce a larger splash on impact compared to fresh water droplets. Both fresh and salt water droplets maintain a linearly positive relation with droplet diameter. The salt water trend line has a slope of 0.53 compared to 0.39 for fresh water.
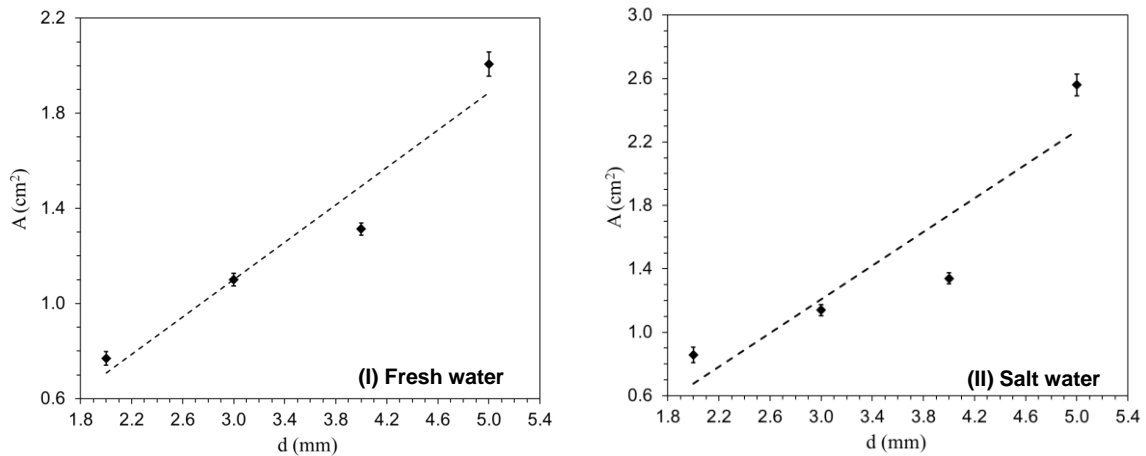
Figure 4.20: Splash area (A) for d = 2, 3, 4, 5 mm droplet upon impact on a cold surface at T_s = -25°C and h = 130 cm. (I) Fresh water (II) Salt water.

Saltwater droplet splashes are typically 2 to 11% larger than fresh water, with droplet diameters from 2 to 4 mm. However, for d = 5 mm a 27% increase in splash area is

measured, which shows that inclusion of salt particles in water is more prone to influence the splash area of bigger droplets than smaller ones.

Figure 4.21 presents a comparison of the thermal behavior of fresh and salt water, at the smallest droplet diameter in the experiments, and with different surface temperatures. For both fresh and salt water droplets, more splash fingers appear at a higher temperature of the cold plate than at lower temperatures.
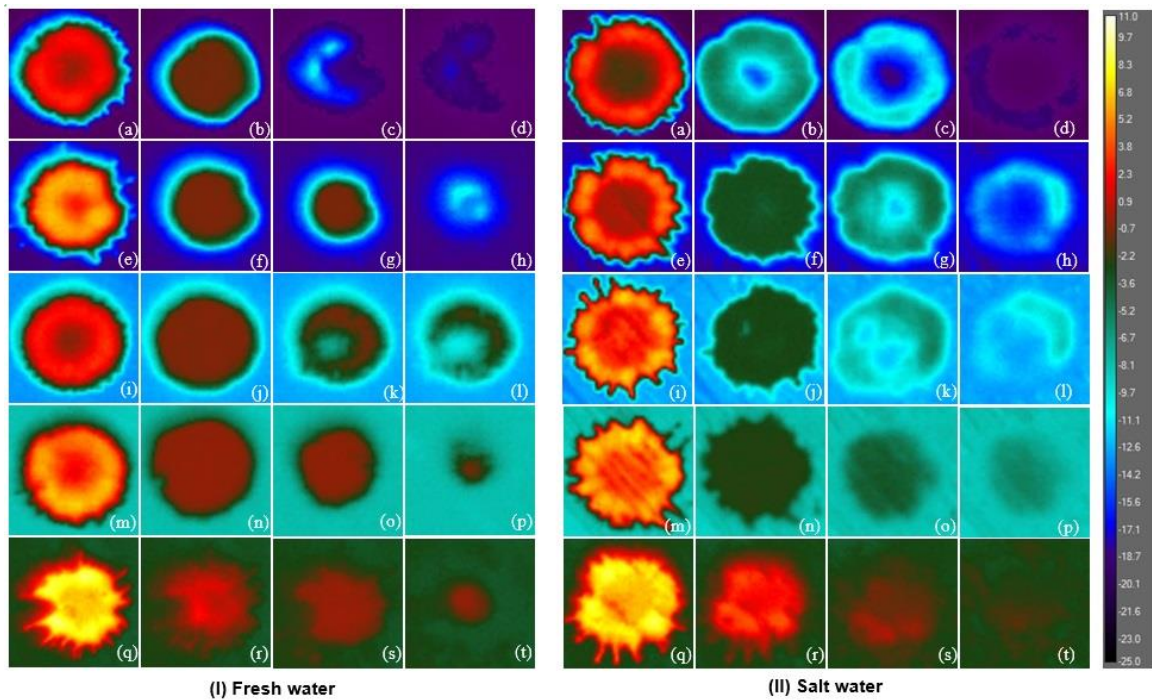
Figure 4.21: Thermal images on impact for d = 2 mm saline droplet falling from h = 130 cm at Ts = -25° C, -20° C, -15° C, -10°C and -5°C (I) Fresh water (II) Salt water.

As illustrated in Fig. 4.21 k and l, for fresh water, the droplet continues to reduce in size from the outside and in some instances, a central region also seems to appear. For d = 2 mm, there is less opportunity to freeze the droplet both from the center and the periphery

in the small freezing time available. For salt water droplets at a later stage of the freezing process, such as in Fig. 4.21 c, g and k of salt water images, central freezing regions appear in the splash zone. Due to the inclusion of salt content, it takes more time for the cold surface to cool down the droplet to its temperature than in the case of fresh water.
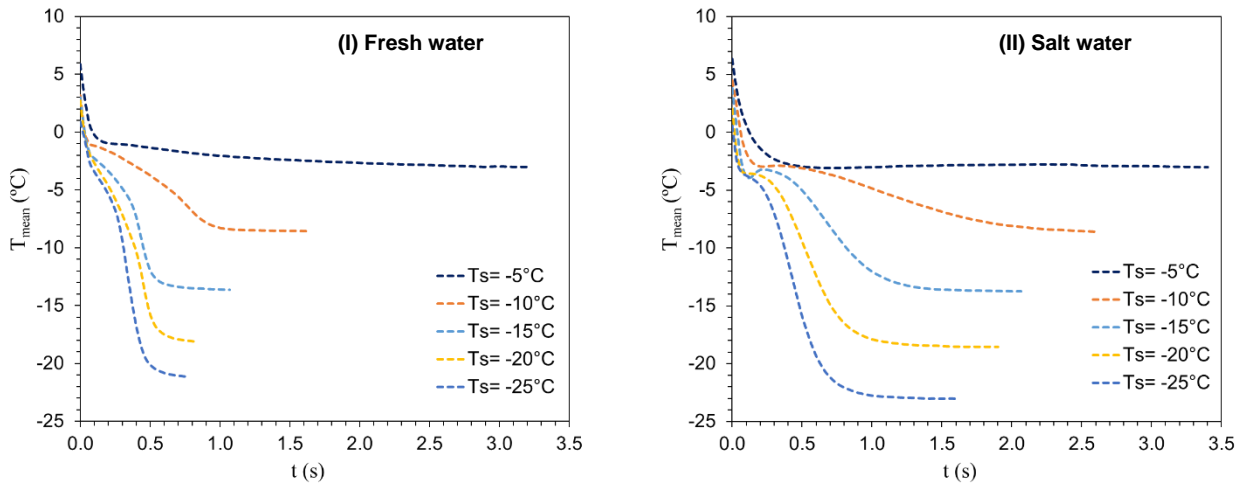
Figure 4.22: Variation of mean temperature for d = 2 mm droplet falling from h = 130 cm at various surface temperature (I) Fresh water (II) Salt water.

More time availability for even the smallest saline droplet splash creates the opportunity to freeze the droplet from the center which first encountered the target surface. The central cooling zones are mostly visible at a lower surface temperature range of -15°C to -25°C. The side by side plots of Fig. 4.22 illustrates that salt water droplets take 0.5 s to 1.0 s longer than fresh water drops to cool and stabilize at the cold plate temperature. Due to the presence of salt particles in saline water, which undergoes continuous salt rejection across the phase change interface, as well as absorbs heat from the cold surface, saline droplets take longer to cool compared to fresh water droplets.

In Fig. 4.23, the R^2 values of linear regression are 0.49 and 0.9 for fresh and salt water, respectively. The values suggest that splash area has a moderate and substantial dependency on the surface temperature for both fresh and salt water droplets. A temperature reduction from -5°C to -25°C, also decreases the splash area for a fresh water droplet by 16.5%. However, for the same size salt water droplets, reducing the temperature caused an increased splash area.
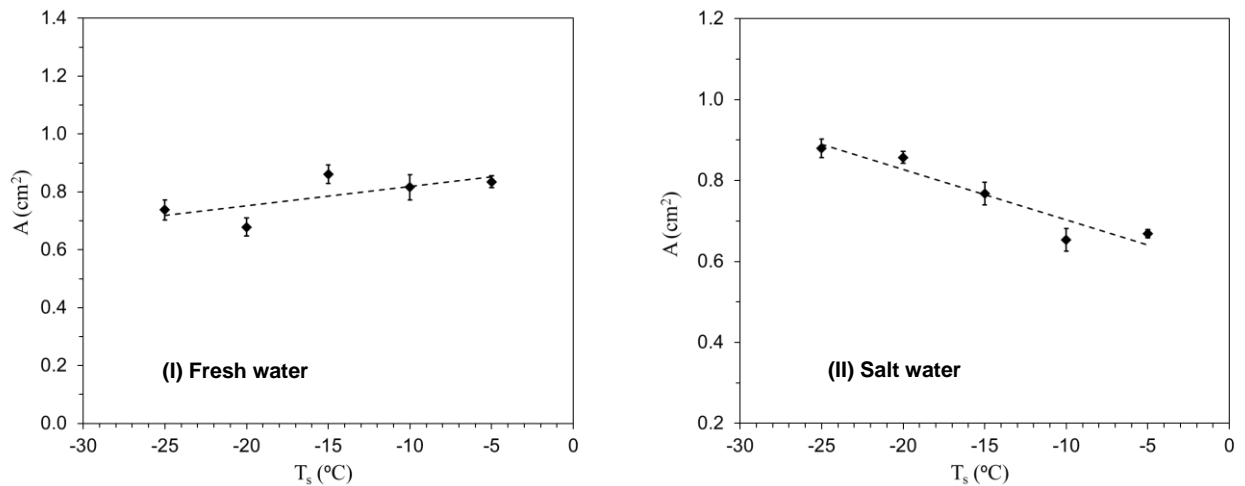
Figure 4.23: Variation of splash area (A) upon impact for d = 2 mm saline droplet falling from h = 130 cm at various surface temperature.

The splash area increased by a maximum of 12% at -25°C. The slower cooling rate of the salt water droplets and salt content in the water is likely the cause of the different behavior of splash area. For the same droplet size, the cooling behavior of fresh and saline water droplets have a lot of dissimilarities. From the physical aspect of the freezing revealed by thermal images, distinguishable behaviors have been observed between fresh and salt water. Salt content in water affects the cooling time of a single drop of water. As the volume

of the droplet increases, the difference in cooling time becomes more noticeable. The contrasting behavior of splash area, at various surface temperature upon impact, is also a noteworthy difference that is visible between fresh and saline water.

Chapter 5: Conclusions and Recommendations

5.1 Conclusions

Marine icing is a critical problem for offshore structures and marine vessels that must be addressed to ensure safe working condition in an arctic environment. In this thesis, two separate experimental investigations were conducted to provide new insights on the physics of marine icing from wave breakup and impact solidification. The appropriate model preparation techniques, control and measurement systems were successfully implemented.

The extent of the breakup of a flat-water jet upon impacting a vertical surface at various angles and velocities were studied experimentally. The change of variables such as jet velocity and attack angle were examined to determine their effect on water sheet breakup. Measurable variables such as sheet height, width and area increased the quantity of breakup. The energy and angle of attack of the water jet at impact affected the water shedding and projectile of the water splash after a breakup. Dimensional and non-dimensional analysis of the results show that jet velocity significantly affects splash size upon breakup. The behavior of the water sheet at impact suggested that high attack angles are beneficial in low-velocity impacts. The jet velocity is the cause of sheet breakup at high velocities and attack angles can be neglected beyond $\theta = 10°$. The results provide valuable new experimental data vessel-wave interaction.

The process of solidification in fresh and salt water droplets after impacting a supercooled surface was experimentally studied. The change of variables such as droplet

size, height and surface temperature were studied to determine their effect on temperature distribution and splash area of fresh and salt water droplets. In fresh water freezing, droplet cooling behavior, splash area and solidification time were mainly affected by the volume of the falling droplets. The larger the droplet, the more time required to solidify and a bigger splash was produced on impact. The change in surface temperature was the key factor affecting the cooling time for fixed falling diameter of both types of droplets. The presence of salt became a more prominent factor on cooling time as the falling droplet size was increased. Distinct variation of splash area in saline drops at various surface temperatures were also exhibited due to the slower cooling time and salt presence.

5.2 Recommendations

This present study developed new experimental equipment to investigate marine icing. A sufficient level of advancement has been obtained in the experimental investigation and test procedures. It is recommended that further experimental research on marine icing in the following areas is needed.

- In this current study, ambient water supply and environment were used in the solidification study. Thus, at lower surface temperature, such as in -15° C to -25° C, the cold plate gathered a lot of ice from the environment and eventually caused the wetting of the surface. This resulted in continuous monitoring and cleaning the surface before each experiment. In a future study, it is recommended to perform the experiments in a controlled environment.

- The water breakup facility should also be taken inside a cold room and controlled water supply from outside can better replicate the fluid breakup scenario as observed in the arctic environment.

- To monitor the temperature distribution of droplets at impact, long wave IR camera were used which does not have high frame rate capability. As the whole phenomenon is fast acting, thermal capture at a high frame rate allow in-depth information on the overall process.

- The impact dynamics of a water droplet on a solid surface can be influenced by a variety of parameters, such as impact velocity, surface tension, viscosity, droplet size, surface temperature and wettability. The use of high speed imaging in the freezing experiment can provide further information on Weber number and Reynolds number and show their effect on a droplet's impact dynamics on a sub-cooled solid surface.

- Further analysis should be performed on estimating the droplet population in the generated water sheet at the impact on a vertical surface. This would provide valuable information on the trajectory of the splash and most importantly the prone locations for marine icing on an offshore structure.

References

Aalbers, A.B. and Poen, G.J., 2015, March. Probabilistic Modelling of Marine Icing: an Estimation Method for Spray Water. In *OTC Arctic Technology Conference*. Offshore Technology Conference.

Bodaghkhani, A., Dehghani, S.R., Muzychka, Y.S. and Colbourne, B., 2016. Understanding spray cloud formation by wave impact on marine objects. *Cold Regions Science and Technology*, *129*, pp.114-136.

Brakel, T.W., Charpin, J.P.F. and Myers, T.G., 2007. One-dimensional ice growth due to incoming supercooled droplets impacting on a thin conducting substrate. *International Journal of Heat and Mass Transfer*, *50*(9), pp.1694-1705.

Bullock, G.N., Obhrai, C., Peregrine, D.H. and Bredmose, H., 2007. Violent breaking wave impacts. Part 1: Results from large-scale regular wave tests on vertical and sloping walls. *Coastal Engineering*, *54*(8), pp.602-617.

Castrejón-Pita, J.R., Castrejón-García, R. and Hutchings, I.M., 2013. High speed shadowgraphy for the study of liquid drops. In *Fluid Dynamics in Physics, Engineering and Environmental Applications* (pp. 121-137). Springer Berlin Heidelberg.

Chuah, Y.K., Lin, J.T. and Yu, K.H., 2016. An Experimental Study on the Heat Transfer of Traveling Airborne Water Droplets in Cold Environment. *Journal of Mechanics*, *32*(02), pp.219-225.

Dehghani, S.R., Muzychka, Y.S. and Naterer, G.F., 2016. Droplet trajectories of wave-impact sea spray on a marine vessel. *Cold Regions Science and Technology*, *127*, pp.1-9.

Forest, T.W., Lozowski, E.P. and Gagnon, R., 2005, June. Estimating marine icing on offshore structures using RIGICE04. In *International Workshop on Atmospheric Icing on Structures (IWAIS), Monreal*.

Fukusako, S., Horibe, A. and Tago, M., 1989. Ice accretion characteristics along a circular cylinder immersed in a cold air stream with seawater spray.*Experimental Thermal and Fluid Science*, *2*(1), pp.81-90.

Fumoto, K. and Kawanami, T., 2012. Study on freezing characteristics of supercooled water droplets impacting on solid surfaces. *Journal of Adhesion Science and Technology*, *26*(4-5), pp.463-472.

Galiev, S.U. and Flay, R.G., 2014. Interaction of breaking waves with plates: the effect of hull cavitation. *Ocean Engineering*, *88*, pp.27-33.

Gent, R.W., Dart, N.P. and Cansdale, J.T., 2000. Aircraft icing. *Philosophical Transactions of the Royal Society of London A: Mathematical, Physical and Engineering Sciences*, *358*(1776), pp.2873-2911.

Guilcher, P.M., Jus, Y., Couty, N., Brosset, L., Scolan, Y.M. and Le Touzé, D., 2014, August. 2D Simulations of Breaking Wave Impacts on a Flat Rigid Wall–Part 1: Influence of the Wave Shape. In *The Twenty-fourth International Ocean and Polar Engineering Conference*. International Society of Offshore and Polar Engineers.

Hellan, Ø., Hermundstad, O.A. and Stansberg, C.T., 2001, January. Designing for wave impact on bow and deck structures. In *The Eleventh International Offshore and Polar Engineering Conference*. International Society of Offshore and Polar Engineers.

Hindmarsh, J.P., Russell, A.B. and Chen, X.D., 2003. Experimental and numerical analysis of the temperature transition of a suspended freezing water droplet. *International Journal of Heat and Mass Transfer*, *46*(7), pp.1199-1213.

Horjen, I., 2015. Offshore drilling rig ice accretion modeling including a surficial brine film. *Cold Regions Science and Technology*, *119*, pp.84-110.

Jin, Z., Wang, Y. and Yang, Z., 2014. An experimental investigation into the effect of synthetic jet on the icing process of a water droplet on a cold surface. *International Journal of Heat and Mass Transfer*, *72*, pp.553-558.

Jung, S., Tiwari, M.K., Doan, N.V. and Poulikakos, D., 2012. Mechanism of supercooled droplet freezing on surfaces. *Nature communications*, *3*, p.615.

Karev, A.R., Farzaneh, M. and Kollár, L.E., 2007. Measuring temperature of the ice surface during its formation by using infrared instrumentation. *International Journal of Heat and Mass Transfer*, *50*(3), pp.566-579.

Kulyakhtin, A., Kulyakhtin, S. and Løset, S., 2013, June. Measurements of Thermodynamic Properties of Ice Created by Frozen Sea Spray. In *The Twenty-third International Offshore and Polar Engineering Conference*. International Society of Offshore and Polar Engineers.

Makkonen, L., 2012. Ice adhesion—theory, measurements and countermeasures. *Journal of Adhesion Science and Technology*, *26*(4-5), pp.413-445.

Myers, T.G. and Hammond, D.W., 1999. Ice and water film growth from incoming supercooled droplets. *International Journal of Heat and Mass Transfer*, *42*(12), pp.2233-2242.

Negeed, E.S.R., Hidaka, S., Kohno, M. and Takata, Y., 2011. Experimental and analytical investigation of liquid sheet breakup characteristics. *International Journal of Heat and Fluid Flow*, *32*(1), pp.95-106.

Obara, T., Bourne, N.K. and Field, J.E., 1995. Liquid-jet impact on liquid and solid surfaces. *Wear*, *186*, pp.388-394.

Ozeki, T., Kitagawa, H., Izumiyama, K., Shimoda, H. and Kosugi, K., 2005. An investigation of sea spray icing and deicing on membrane structures. In *Proceedings of 11th International Workshop on Atmospheric Icing of Structures, Montreal, Canada, Paper IW76* (p. 4).

Palacios, E., Nogueira, J., Rodríguez, P.A. and Lecuona, A., 2009. Experimental characterization of the spreading and break-up of liquid flat-fan sheets discharging in a low-density atmosphere and application to BrLi solutions. *Experiments in Fluids*, *46*(2), pp.331-342.

Prodi, F., Levi, L., Franzini, A. and Scarani, C., 1982. Crystal size and orientation in ice grown by droplet accretion in wet and spongy regimes. *Journal of the Atmospheric Sciences*, *39*(10), pp.2301-2312.

Ren, N. and Marshall, A.W., 2014. Characterizing the initial spray from large Weber number impinging jets. *International Journal of Multiphase Flow*, *58*, pp.205-213.

Rodrigues, N.S., Kulkarni, V., Gao, J., Chen, J. and Sojka, P.E., 2015. An experimental and theoretical investigation of spray characteristics of impinging jets in impact wave regime. *Experiments in Fluids*, *56*(3), pp.1-13.

Ryerson, C.C., 2011. Ice protection of offshore platforms. *Cold Regions Science and Technology*, *65*(1), pp.97-110.

Strub, M., Jabbour, O., Strub, F. and Bédécarrats, J.P., 2003. Experimental study and modelling of the crystallization of a water droplet. *International Journal of Refrigeration*, *26*(1), pp.59-68.

Thoroddsen, S.T., Etoh, T.G. and Takehara, K., 2008. High-speed imaging of drops and bubbles. *Annu. Rev. Fluid Mech.*, *40*, pp.257-285. Wahono, S., Honnery, D., Soria, J. and Ghojel, J., 2008. High-speed visualisation of primary break-up of an annular liquid sheet. *Experiments in fluids*, *44*(3), pp.451-459.

TO, K. and Wood, R., 2015. An approximation for homogeneous freezing temperature of water droplets. *Atmospheric Chemistry & Physics Discussions*, *15*(21).

Weymouth, G., Hendrickson, K., Yue, D.K., O'Shea, T., Dommermuth, D., Adams, P. and Valenciano, M., 2007, June. Modeling breaking ship waves for design and analysis of naval vessels. In *DoD High Performance Computing Modernization Program Users Group Conference, 2007* (pp. 440-445). IEEE.

Wu, D., Guillemin, D. and Marshall, A.W., 2007. A modeling basis for predicting the initial sprinkler spray. *Fire safety journal*, *42*(4), pp.283-294.

Yang, G., Guo, K. & Li, N., 2011. Freezing mechanism of supercooled water droplet impinging on metal surfaces. *International Journal of Refrigeration,* pp. 2007-2017.

Yettou, E.M., Desrochers, A. and Champoux, Y., 2006. Experimental study on the water impact of a symmetrical wedge. *Fluid Dynamics Research*,*38*(1), pp.47-66.

Zakrzewski, W.P., 1987. Splashing a ship with collision-generated spray. *Cold Regions Science and Technology*, *14*(1), pp.65-83.